

Saharan dust impacts on the surface mass balance of Argentière Glacier (French Alps)

Léon Roussel^{1, 2, 3}, Marie Dumont^{1, 2, 3}, Marion Réveillet^{4, 2}, Delphine Six^{4, 2}, Marin Kneib^{4, 2, 5, 6}, Pierre Nabat^{7, 3}, Kévin Fourteau^{1, 2, 3}, Diego Monteiro^{1, 2, 3}, Simon Gascoin^{8, 3}, Emmanuel Thibert^{4, 2}, Antoine Rabatel^{4, 2}, Jean-Emmanuel Sicart^{4, 2}, Mylène Bonnefoy^{4, 2}, Luc Piard^{4, 2}, Olivier Laarman^{4, 2}, Bruno Jourdain^{4, 2}, Mathieu Fructus^{1, 2, 3}, Matthieu Vernay^{1, 2, 3}, and Matthieu Lafaysse^{1, 2, 3}

¹Centre d'Études de la Neige, Centre Nationale Recherches Météorologiques (CNRM), Météo-France/CNRS, Grenoble 38000, France

²Université Grenoble Alpes, Grenoble 38000, France

³Université de Toulouse, Toulouse 31000, France

⁴Institut des Géosciences de l'Environnement (IGE, UMR 5001), CNRS/IRD/INRAE/Grenoble INP, 38400 Saint Martin d'Hères, France

⁵Laboratory of Hydraulics, Hydrology and Glaciology (VAW), ETH Zurich, Zurich, Switzerland

⁶Swiss Federal Institute for Forest, Snow and Landscape Research (WSL), bâtiment ALPOLE, Sion, Switzerland

⁷Centre Nationale Recherches Météorologiques (CNRM), Météo-France, CNRS, Toulouse 31000, France

⁸Centre d'Etudes Spatiales de la Biosphère (CESBIO), CNRS/IRD/CNES/UT3, Toulouse 31000, France

Correspondence: Léon Roussel (leon.roussel@meteo.fr)

Abstract. Saharan dust deposits frequently turn alpine glaciers orange and darken their surface. Together with other light-absorbing particles, mineral dust reduces snow albedo, increases snow melt rate, and lowers the surface mass balance of glaciers. Since the surface mass balance drives the evolution of alpine glaciers, assessing the impact of impurities helps to understand their current and future evolution. The location of impurities within the snowpack and their effect on snow albedo can be estimated through physical modelling. In this study, we quantified the impact of dust, taking into account mineral dust and black carbon in snow, on the Argentière Glacier over the period 2019-2022. Our results show that during the three years preceding 2022, the contribution of mineral dust to the annual decrease in surface mass balance was between 0.31-0.45 m w.e., while it reached the double in 2022 with 0.63 m w.e. [0.54, 0.69] (median, [Q10-Q90]), and up to 1.2 m w.e. [0.9, 1.4] at specific locations. The impact of dust in snow was unevenly distributed over the glacier, especially in 2022. The highest simulated impacts occurred where firn layers from previous years were exposed after the total melt of the snowpack of the previous winter. The gravitational redistribution of the snow from avalanches was not taken into account, which can reduce the impact of dust at specific locations. Increasing the modelled scavenging efficiency of black carbon can double the impact of dust alone at the glacier scale. In general, the contribution of mineral dust to the melt represents between 8 and 16 % of Argentière Glacier summer melt depending on the year. Hence, we recommend accounting for impurities to simulate the distributed surface mass balance of glaciers.

1 Introduction

In the European Alps, the surface mass balance (SMB) is a key component of the evolution of glaciers, as it controls the total mass budget of alpine glaciers (Cuffey, Paterson, 2010). When the surface of a glacier is at the melting point, a positive surface energy budget enables the glacier surface to melt. For alpine glaciers, the variability of this surface energy budget is mainly driven by shortwave radiation, *e.g.*, Sicart et al. (2008). In mountainous areas, the incoming shortwave radiation strongly varies with the local topography (Arnold et al., 2006; Robledano et al., 2022). At the glacier surface, the shortwave radiation budget is modulated by the snow and ice albedo (Warren, 1982; Gardner, Sharp, 2010). The albedo of snow is determined, among other parameters, by snow properties and light-absorbing particles (LAPs) such as mineral dust (dust) or black carbon (BC). The evolution of LAP concentration at the glacier surface therefore modulates the glacier SMB.

The impact of LAPs is not restricted to the European Alps. By lowering the albedo, LAPs contribute to significantly accelerate snow and glacier melt around the world, *e.g.*, Ménégoz et al. (2014); Ginot et al. (2014); Magalhães et al. (2019); Sarangi et al. (2020); Gilardoni et al. (2022); Gunnarsson et al. (2023); Menounos et al. (2025). In the Andes and High Mountain Asia, high LAP deposition fluxes and high melt impacts motivated these studies. In the European Alps, only a few studies quantified the impact of LAPs on glaciers, while the impact of LAPs on the melt of seasonal snow has been quantified by numerous studies, *e.g.*, Di Mauro et al. (2019); Tuzet et al. (2020); Réveillet et al. (2022); Di Mauro et al. (2024). For instance, on average over the past 40 years, the presence of LAPs in snow has advanced the snow melt-out date by 18 days in the French Alps, and even more at high elevations (more than 20 days at 3,000 m a.s.l., Réveillet et al., 2022).

The radiative impact of BC has often been in the spotlight, *e.g.*, Bond et al. (2013). However, BC emissions and depositions on the snowpack have decreased from the end of the 20th century in the European Alps, *e.g.*, Sun et al. (2020); Grange et al. (2020); Réveillet et al. (2022). Mineral dust also has a significant impact on snow melt (Skiles et al., 2018) and on glacier melt, *e.g.*, Sarangi et al. (2020). Regarding mineral dust depositions, Europe is mainly influenced by Saharan dust transport, which is the main contributor that represents between 50 and 70 % of the total annual dust depositions (Ginoux et al., 2001). Above 2,000 m a.s.l. in the French Alps, the impact of dust alone has advanced the snow-melt out date by more than 10 days (Réveillet et al., 2022). Réveillet et al. (2022) showed that the impact of BC and dust increased with elevation, but this increase was more pronounced for dust. Moreover, Dumont et al. (2020) also showed that the radiative forcing of dust presented large topographic gradients. This increase in the impact of dust with elevation is due to several reasons. First, the late depositions of dust in the European Alps with intense deposition events occurring usually after March (*e.g.*, Moulin et al. (1998); Collaud Coen et al. (2004)) impact less the melt at low elevations that starts earlier. Second, for the highest elevations, the melting period is longer and occurs in spring and summer that are period associated with higher shortwave radiation than winter (Dumont et al., 2020). Thus the impact of dust on the overall glaciers mass balance should be accurately quantified.

Quantifying the specific contribution of LAPs to the SMB of an entire glacier could be achieved using physical modelling. Indeed, by representing different physical processes, physically based models can simulate snow and ice evolution. Some models directly account for the impacts of the LAPs, *e.g.*, the snow model SURFEX/ISBA-Crocus (Vionnet et al., 2012; Tuzet et al., 2017) or the Community Land Model (Flanner et al., 2007). To our knowledge, only one study modelled and quantified

the time evolution of the impact of dust on the SMB of a glacier in the European Alps (Gabbi et al., 2015). The authors modelled the SMB at two locations on the Clariden Glacier in Switzerland over a century. They quantified the long-term impact of dust and BC with the re-exposure of contaminated firn layers and showed that Saharan dust lowered the mean annual SMB by 0.03-0.06 m w.e. and black carbon by 0.2-0.3 m w.e. They found that annual melt rates were amplified by only 2 % due to the presence of mineral dust and by 10 % due to the presence of black carbon. However, this study did not assess the impact of dust on the SMB over an entire glacier area despite the small surface area of this glacier. In addition, Clariden Glacier is located in the northern part of the European Alps, which is less exposed than the southern part to Saharan dust deposition, *e.g.*, Baladima (2021). Hence, we do not expect these results to be directly transferable to other alpine glaciers.

This study therefore focuses on the following research question: what is the impact of mineral dust on the SMB of an alpine glacier? To address this question, we selected the Argentière Glacier during the period 2019-2022. Being part of the French glacier observatory GLACIOCLIM, Argentière Glacier is closely monitored and studied (*e.g.*, Vincent et al., 2009; Rabatel et al., 2018; Kneib et al., 2024b). The year 2022 was characterized by a strong precipitation deficit and heat waves in the French Alps (Mittelberger et al., 2024; Gascoin et al., 2024), leading to an exceptional mass loss of alpine glaciers in spring and summer (Six et al., 2023; Berthier et al., 2023; Cremona et al., 2023). In addition, a significant Saharan dust deposition event occurred on 16 March 2022 (Gascoin et al., 2024). These events were preceded by notable Saharan dust deposition events in February 2021 (Dumont et al., 2023).

In this context, we simulated the distributed SMB of Argentière Glacier using the snow model SURFEX/ISBA-Crocus (Vionnet et al., 2012; Lafaysse et al., 2017; Vernay et al., 2022), which includes the Two-streAm Radiative TransfEr in Snow (TARTES, G. Picard, Q. Libois, 2024) with an explicit representation of LAPs in snow (Tuzet et al., 2017). This model had already been used to model alpine glacier SMB, *e.g.*, Dumont et al., 2012; Réveillet et al., 2018. We performed an ensemble of simulations to account for meteorological forcing uncertainties. The resulting SMB were evaluated using point SMB measurements from in-situ surveys, glacier surface facies derived from Sentinel-2 images, and distributed SMB retrieved from satellite observation and modelling Kneib et al. (2024b). We also performed control simulations by deactivating the effect of mineral dust on albedo to quantify the variation of the SMB that can be attributed to dust depositions in snow.

2 Material and Methods

2.1 Study site and topography

Argentière Glacier (45°57'N, 7°00'E) is located in the Mont-Blanc mountain range in France. The extent of the glacier is 11 km² in 2022, ranked 19th largest glacier in the European Alps, and the studied glacier area ranges from 3,600 to 2,100 m a.s.l. The main flowline of the glacier is 8 km long. This glacierized valley is mainly north-west facing (Fig. 1d) and surrounded by multiple peaks above 3,800 m a.s.l. Argentière Glacier surface can be impacted by Saharan events, as shown in Fig. 1a which illustrates this phenomenon in August 2021, with an orange coloration observed in the glacier accumulation area. A dark orange color was visible in August 2022 (Fig. 1b), associated with an extreme negative mass balance in 2022 (Fig. 1c).

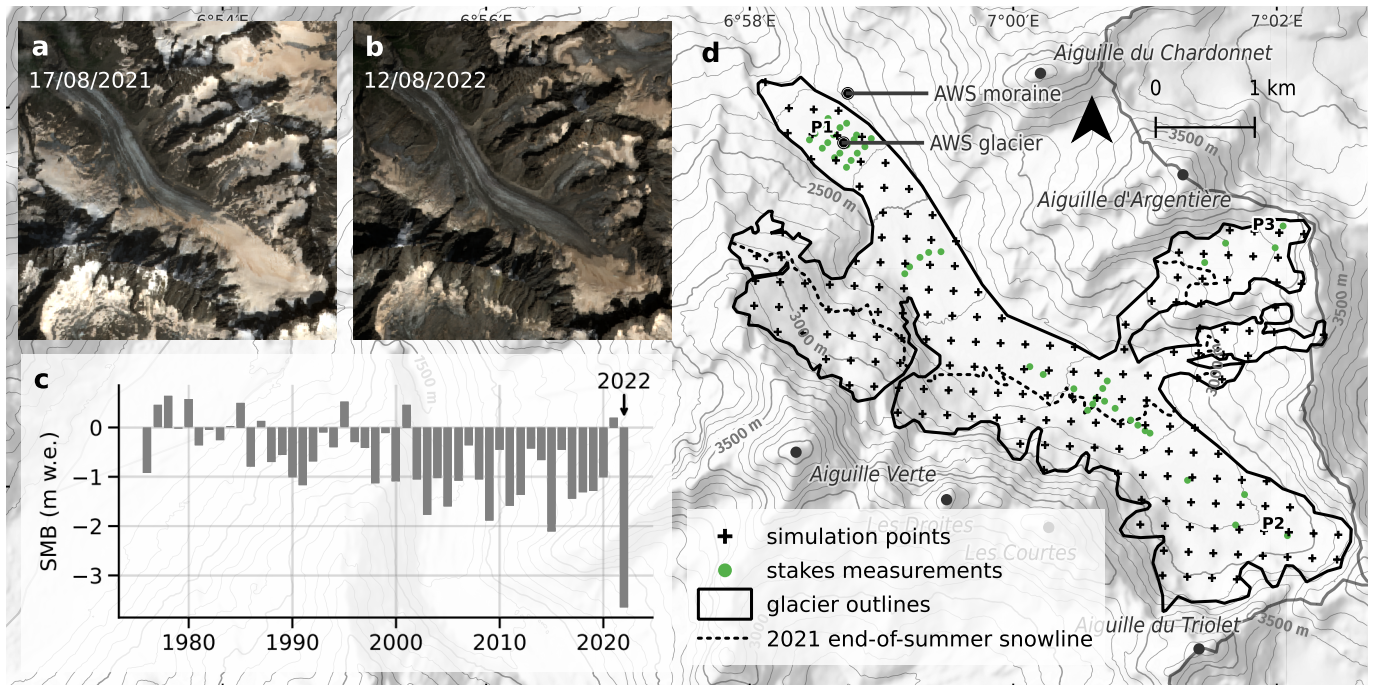


Figure 1. (a, b) True color Sentinel-2 images of Argentière Glacier on (a) 17/08/2021 and (b) 12/08/2022 (Section 2.2.2). (c) Annual glacier-wide surface mass balance of Argentière Glacier over the period 1976–2022 from the French glacier monitoring service GLACIOCLIM. (d) Map of Argentière Glacier. The 2021 end-of-summer snowline was manually derived from the 27/08/2021 Sentinel-2 image. Details of the SMB evolution at point P1, P2 and P3 are shown in Fig. 5. Background map from MapTiler.

In this study, we used constant outlines of the glacier from the year 2019 (black line in Fig. 1d), and a digital elevation model (DEM) at a 10 m resolution from Copernicus. The DEM was used here for meteorological data downscaling, *e.g.*,
 85 computation of direct solar radiation using a topographic mask (see Section 2.3.3). Simulation points (black crosses in Fig. 1d) were extracted from a two-dimensional grid at a horizontal resolution of 250 m using the Lambert 93 coordinate system (EPSG:2154).

2.2 Evaluation data

2.2.1 Point SMB measurements

90 Argentière Glacier is regularly monitored since 1975 by the GLACIOCLIM observatory (<https://glacioclim.osug.fr/>). Winter accumulation measurements from autumn to spring and summer melt measurements from spring to autumn provide observed point winter and summer SMB along three ablation profiles of the main tongue (at 2,400, 2,500 and 2,700 m a.s.l.) and in the two main accumulation areas (green points in Fig. 1d). Point SMB refers to the local surface mass balance, whereas glacier-wide SMB refers to the SMB integrated over the entire surface area of the glacier.

95 In this study, the annual SMB of year N refers to the hydrological year N, *i.e.*, 1st October N-1 to 30 September N, and is expressed in metres of water equivalent (m w.e.). The accuracy of the point SMB measurements is estimated to be around 0.2 m w.e. (Thibert et al., 2008). Point winter SMB were used to adjust precipitation (Section 2.3.5). Point summer SMB measurements were used to evaluate the simulated summer SMB at the closest simulation grid point (Section 3.1).

2.2.2 Sentinel-2 optical satellite images

100 In this study, Sentinel-2 satellite (S2) images were used to (i) derive the surface type and mean snowline elevation to evaluate the simulations; and (ii) infer the glacier ice albedo. S2 images are optical, high-resolution and multispectral satellite images with a revisit time of at most 5 days. Here, we used bottom-of-atmosphere reflectances from Theia from the tile T32TLR containing Argentière Glacier (see Data Availability). Those reflectances were corrected using the MAJA level-2A processor that performs topographic and atmospheric corrections (Hagolle et al., 2015). We used the reflectance of all spectral bands at
105 10 and 20 m spatial resolution. Bands at 10 m spatial resolution were resampled to 20 m with the cubic method. To avoid using images containing clouds, we visually selected a total of 21 cloud-free images acquired between May and October of the years 2019 to 2022 (detail on the date can be found in the Appendix Table B1). We selected only images between May and October because the glacier was often fully snow-covered outside of this period, which was not helpful for the evaluation.

2.2.3 Surface type derived from Sentinel-2 data

110 To evaluate our glacier simulations, we used a surface type classification derived from S2 images. The classification method splits the pixels into three different classes: ice, snow, and "not-glaciated". The latter refers to pixels containing shadows, rocks, moraine debris, or liquid water. To develop the classification method, we manually labelled 8,639 pixels using 216 polygons (5,209 snow pixels, 1,594 ice, and 1,836 not-glaciated) extracted in the S2 images of Argentière Glacier. Appendix Fig. B1 shows the distribution of the pixels depending on variable R_{B4} , NDSI and RGND, where R_{B_i} is the S2 reflectance of band
115 i , $NDSI = \frac{R_{B3} - R_{B11}}{R_{B3} + R_{B11}}$ and $RGND = \frac{R_{B4} - R_{B3}}{R_{B4} + R_{B3}}$. The central wavelengths of bands $B3$, $B4$ and $B11$ are respectively 560, 665 and 1610 nm. Based on the distribution of the labelled pixels and the optical properties of snow and ice (Warren, 1984; Dozier, 1989; Painter et al., 2013; Di Mauro et al., 2015; Gascoin et al., 2019; Flanner et al., 2021; Dumont et al., 2020; Di Mauro et al., 2024), the classification method was defined using three thresholds: a pixel was classified as 'not-glaciated' if $R_{B4} < 0.12$ or $NDSI < 0.5$, and as snow or ice otherwise. In the last case, a pixel was classified as snow if $R_{B4} > -6.0 \times RGND + 0.525$ and
120 as ice otherwise.

For each simulation point and S2 image, an S2 surface type was determined using the previous classification. The S2 surface type was snow (ice) if the snow (ice) pixels are in larger numbers in the 7x7 surrounding pixels around the simulation point, otherwise the S2 surface type was not defined. This S2 surface type was compared with the simulated surface type in Section 3.1 with the surface type error rate (frequency of error between the simulated and S2 surface types at all simulation points).

125 2.2.4 Sentinel-2 mean snowline elevation

For each selected satellite image, an S2 mean snowline elevation was computed (as illustrated in Appendix Fig. B2). For each image, we binned all classified pixel as ice or snow into 100 m elevation classes. Bin b_i refers to the bin between elevations E_i and $E_i + 100$. Then, we defined b_j as the lowest elevation bins with more pixels classified as snow than ice. Hence, bin b_{j-1} contains more pixels classified as ice than as snow. Finally, we computed the mean snowline elevation, between elevation
130 $E_j - 50$ and $E_j + 50$, using a linear interpolation between the snow ratios in bins b_{j-1} and b_j , as the elevation for which the snow ratio would be 50 %. This S2 snowline elevation was compared with the simulated snowline elevation in Section 3.1.

2.2.5 Sentinel-2 broadband ice albedo

The ice albedo was a parameter of our surface mass balance model. We inferred this parameter using S2 images and simulated ice spectra from the SNICAR radiative transfer model (Whicker et al., 2022). We computed eight spectral albedos of ice
135 reflectance with different BC concentrations (75 to 1,000 ng g^{-1}), at 10 nm resolution from 205 to 4,995 nm with mid-latitude, clear-sky, summer irradiance conditions. These SNICAR spectra were used to interpolate between the S2 bands. For each S2 pixel classified as ice in the 21 selected images, we affected the SNICAR spectrum that minimized the RMSE between the SNICAR spectra and the S2 spectrum of the pixel. The spectral albedos from SNICAR were then weighted by the incident irradiance to obtain broadband albedos. We finally computed the ice albedo by averaging the SNICAR broadband albedo
140 related to all the ice pixels. The resulting ice albedo on the 21 selected S2 images was 0.23 with a standard deviation of 0.05. This method is rather simple since we here aimed to quantify the impact of dust in snow, not in ice. Nevertheless, the sensitivity to this parameter was investigated in Section 3.3.

2.2.6 Broadband snow albedo derived from Sentinel-2 reflectances

Using all images of Table B2, we compared the modeled broadband albedo at noon, and the observed broadband albedo derived
145 from Liang et al. (2003), *i.e.*, $S2 \text{ albedo} = 0.356 * R_{B2} + 0.130 * R_{B4} + 0.373 * R_{B8} + 0.085 * R_{B11} + 0.072 * R_{B12} - 0.018$ where R_{B_i} is the reflectance of Sentinel-2 band i . Appendix Fig. B3 shows this comparison. Only the points where the surface type (Section 2.2.3) was snow for both the model and S2 were used.

However, this comparison of absolute albedo has to be taken with cautious. Indeed, there are several limitations. First, the reflection of snow is not isotropic (*e.g.*, Dumont et al. (2010)), *i.e.*, depends on the observation angle, and also varies with the
150 solar zenith angle. Second, the uncertainties of the reflectance retrievals in complex terrain may be too high to estimate the accuracy of the simulated albedo, *e.g.*, Cluzet et al. (2020). This is also highlighted on Appendix Fig. B3a where the computed S2 broadband albedo strongly depends on the slope.

2.2.7 Surface mass balance from Pléiades images

Following Kneib et al. (2024b), surface velocity and elevation change maps were extracted from Pléiades 4 m resolution
155 DEMs and 0.5 m resolution ortho-images to estimate the distributed SMB of Argentière Glacier and its uncertainties at 20 m

resolution for the period 08/09/2018 to 05/10/2022. Elevation change was obtained using six Pléiades DEMs from 08/09/2018, 25/08/2019, 17/09/2020, 30/09/2020, 15/08/2021 and 05/10/2022, and the ice flux was inverted from the 2012-2022 distributed surface velocity using three approaches and ice thickness scenarios to obtain the distributed SMB. In Kneib et al., 2024b, similar inversions for the period 2012-2021 were evaluated against the mean annual point SMB (described in 2.2.1). For the
160 three inversion approaches, the RMSE was lower than 1 m w.e. yr^{-1} , showing good agreement between the resulting Pléiades annual SMB and point measurements.

Ultimately, in this study we used the mean of the resulting Pléiades SMB and the uncertainties of each of the three inversion approaches as our reference distributed SMB (Kneib et al., 2024b). We extracted the closest Pléiades SMB for each simulation point to evaluate the simulated SMB in Section 3.1.

165 2.3 Meteorological data

2.3.1 LAPs deposition fluxes

Mineral dust (dust) and black carbon (BC) hourly deposition fluxes were obtained from the CNRM-ALADIN63 regional climate model driven by the ERA5 reanalysis (Nabat et al., 2020). The prognostic aerosol scheme of ALADIN is called TACTIC (Tropospheric Aerosols for Climate In CNRM, coming from Morcrette et al. (2009) and used in Michou et al. (2015, 2020)).
170 The domain of the model included the Saharan desert with a southern limit roughly corresponding to $+15^{\circ}\text{N}$, as shown in Fig. 1 of Nabat et al. (2020). The emissions of dust were computed by the model as a function of surface wind and soil characteristics (Nabat et al., 2020). Then, mineral dust was a prognostic variable of the model subject to atmospheric processes (transport and deposition). Anthropogenic and biomass burning emissions (including BC) were based on monthly inventories varying from year to year, namely the CEDS v2021-04-21 dataset for historical anthropogenic emissions (O'Rourke et al., 2021) up to
175 2019, extended up to 2022 following the study of Lamboll et al. (2021), and the GFED4.1s dataset (Randerson et al., 2017) for biomass burning emissions. The horizontal grid resolution of the CNRM-ALADIN63 outputs is 12.5 km. Only the nearest grid point output was used for all simulation points. This point was around 2 km from the glacier in a south-west direction. Over the complete simulation period, the mean dust and BC deposition fluxes of this nearest point were respectively $11.4 \text{ g m}^{-2} \text{ yr}^{-1}$ and $0.038 \text{ g m}^{-2} \text{ yr}^{-1}$. When considering the 3×3 CNRM-ALADIN63 grid points around this nearest point, the
180 mean and standard deviation of the fluxes were $10.3 (\pm 2.3) \text{ g m}^{-2} \text{ yr}^{-1}$ and $0.0433 (\pm 0.011) \text{ g m}^{-2} \text{ yr}^{-1}$. ALADIN wet and dry depositions were redistributed with respect to the SAFRAN precipitation as in Réveillet et al. (2022), *i.e.*, wet depositions when SAFRAN precipitations are positive, dry depositions otherwise.

LAPs deposition fluxes from ALADIN have been compared with in situ measurements in Tuzet et al. (2020) and their impacts on the snow melt-out date have been evaluated in Réveillet et al. (2022) using MODIS snow products. Moreover,
185 Dumont et al. (2023) includes a dust mass measurement on Argentière Glacier during the extreme dust deposition event of February 2021. They measured 1.70 g m^{-2} of mineral dust deposition at 2,700 m a.s.l. on 08/02/2021 (measurement integrating the depositions from 05/02/2021 to 08/02/2021). On the other hand, the ALADIN model deposited in total 2.37 g m^{-2} of dust from 05/02/2021 to 08/02/2021 at the nearest grid point from Argentière Glacier. Both values have the same order of magnitude,

which is sufficient to assess the reliability of the model during this event given the difference in spatial resolution between the
190 observation (sampling over an area of 105 cm²) and the simulation (with a spatial resolution of 12 km). The uncertainty related
to the LAPs deposition fluxes is evaluated in Section 3.3 and discussed in Section 4.1.

2.3.2 Automatic weather stations

Two automatic weather stations (AWS) were located at the surface and on the right-hand side moraine with respect to the
glacier flow of Argentière Glacier (Fig. 1d). The glacier AWS was located on the lowest part of the glacier (about 2,400 m
195 a.s.l.), during summer 2021 and recorded every 15 minutes from 20/05/2021 to 22/10/2021. The moraine AWS was maintained
permanently and data was recorded continuously every 30 minutes from 01/01/2015 to 30/09/2022. The elevation difference
between the two AWS is around 70 m, and they are located around 500 m apart (detailed location in Fig. 1d). Among other
parameters, both AWS measured incoming shortwave radiation SW (W m⁻²), incoming longwave radiation LW (W m⁻²), air
temperature at 2 metres (K or °C) and wind speed (ms⁻¹). All measurement time series were averaged to a time-step of 1
200 hour, that is the time-step of the SAFRAN data (Section 2.3.3). The measurement devices and the associated measurement
uncertainties from the manufacturers were listed in Appendix Table C1. A comparison of the measured air temperatures is
presented in Appendix Fig. C1 when both stations recorded. This comparison is used in Section 2.3.4.

2.3.3 SAFRAN data

The SAFRAN atmospheric reanalysis (Vernay et al., 2022) combines meteorological information at the mountain massif scale
205 (here typically 1,000 km² for the Mont-Blanc massif) from numerical weather prediction (ERA-40 reanalysis from 1958
to 2002, ARPEGE from 2002 to 2021) and in situ meteorological surface observations (2 m air temperature and humidity,
10 m wind, 24 h cumulative precipitations). SAFRAN provides hourly meteorological data (2 m air temperature and specific
humidity, wind speed and direction, rainfall and snowfall rate, longwave incoming radiation, shortwave direct and diffuse
radiations) with a 300 m vertical resolution. Those data were extracted from 01/08/2008 to 30/09/2022 and interpolated at
210 each simulation point using their exact elevation following Revuelto et al. (2018). Moreover, direct shortwave radiation was
masked using an illumination mask at 5° resolution computed for each simulation point. Examples of illumination masks and
spatialized mean shortwave radiations are presented in Appendix Fig. C3.

Four SAFRAN variables (air temperature, wind, longwave and shortwave radiations) were bias-corrected based on the ob-
served variables at the moraine AWS. For each variable $V(t)$, for each season s from summer 2015 (winter from October to
215 April, summer from May to September), we computed the bias $b^s = \mu_{V_{\text{saf}}} - \mu_{V_{\text{obs}}}$ for additive variables and $b^s = \mu_{V_{\text{saf}}} \div \mu_{V_{\text{obs}}}$
for multiplicative variables, between the mean of the SAFRAN massif-scale analysis $\mu_{V_{\text{saf}}}$ and the mean of the moraine
AWS observation $\mu_{V_{\text{obs}}}$ (numeric values in Appendix Fig. C2). This enabled seasonally bias-correcting of the SAFRAN vari-
ables at each time-step t following $V_{\text{saf, bias-corr.}}^s(t) = V_{\text{saf}}^s(t) - b^s$ if the variable is additive (air temperature, longwave) and
 $V_{\text{saf, bias-corr.}}^s(t) = V_{\text{saf}}^s(t)/b^s$ if the variable is multiplicative (wind, shortwave). This correction was propagated to all simulation
220 points. It ensured that: (i) on a seasonal scale, the meteorological conditions extracted on the full massif scale did indeed reflect
the conditions in the vicinity of the glacier; (ii) the SAFRAN variables and the observed variables were bias-corrected, which

was an hypothesis needed to later apply stochastic perturbations (Section 2.3.6). Two more adjustments were applied to the SAFRAN data in Sections 2.3.4 and 2.3.5.

2.3.4 SAFRAN temperature adjustment

225 The SAFRAN reanalysis assimilates exclusively observations outside of glacierized areas, so we adjusted the SAFRAN air temperature T which is an ambient, *i.e.* off-glacier air temperature. A difference was observed between both AWS in the case of a high air temperature (above 3.5 °C, Appendix Fig. C1). More precisely, the temperatures measured at the glacier AWS were lower than those at the moraine AWS. This difference for high temperature could be due to cooling from the ice surface or to katabatic down-glacier winds (Sicart et al., 2008; Shea, 2010; Shaw et al., 2023, 2024). A similar pattern was shown by
 230 Shaw et al. (2023) in their Supplementary Fig. S5. In our case, the temperature sensitivity above 3.5 °C was $TS = 0.76$ (K/K), which means that for every increase in 1 °C above 3.5 °C for temperatures outside the glacier, the temperature on the glacier only increased by 0.76 °C. Therefore, we adjusted the SAFRAN temperature T^* , above $T_0 = 3.5$ °C without any upper bound, according to

$$T^* = \begin{cases} TS \cdot (T - T_0) + T_0 & \text{if } T > T_0 \\ T & \text{otherwise} \end{cases} \quad (1)$$

235 2.3.5 SAFRAN solid precipitation adjustment

Using SAFRAN precipitation data systematically underestimated the winter SMB of French alpine glaciers at high elevations (Gerbaux et al., 2005; Dumont et al., 2012; Réveillet et al., 2018; Vionnet et al., 2019; Gilbert et al., 2023). To address this issue, previous studies applied a correction factor to align the total winter precipitation with the observed winter SMB. This correction also accounted for the wind-blown snow redistribution. However, this approach did not account for winter melting
 240 events, which have become more frequent in recent years (*e.g.*, a winter SMB of -1.44 m w.e. was measured punctually at the bottom of the main tongue at 2,400 m a.s.l. of Argentière Glacier in 2022) and is therefore no longer suitable.

Thus, in this study, for a given winter, at a given point with an observed winter SMB, we associated the closest simulation point and its simulated winter SMB b_{mod} (m w.e.) with the initial solid precipitations sp . The targeted simulated winter SMB b_{mes}^* (m w.e.) with corrected solid precipitations should be equal to the winter SMB measurement b_{mes} (m w.e.), hence

$$245 \quad b_{mes} = b_{mod}^* = K \times sp - M_{winter} = K \times sp - (sp - b_{mod}) \quad (2)$$

where K is the multiplicative factor of this study at a given point and for a given winter, sp (m w.e.) the sum of the initial winter solid precipitation, $M_{winter} = sp - b_{mod}$ the simulated melt during the winter (m w.e.). Here, we hypothesized that the simulated melt M_{winter} corresponded to the measured melt. Isolating K in Equation 2 gave

$$K = 1 + \frac{b_{mes} - b_{mod}}{sp} \quad (3)$$

250 Using Equation 3, we calculated the factors K for the winters 2018-2019 to 2021-2022 for all available point winter SMB (Appendix Fig. C2). Because more measurements were made on the lowest part of the glacier, and to avoid an overestimated

impact of these on the upper part, we averaged all the K factors (all winters, all points) over 100 m bins. To obtain the final factors used in this study, we interpolated the aggregated factors K with a polynomial fit of the order one depending on elevation.

255 The final resulting factors ranged from 1.25 to 1.75 and increased with elevation. The explicit equation was $K = 2.03 \times 10^{-4} \cdot (E - 2000) + 1.38$ (black dashed line in Appendix Fig. C2), where E is the elevation (m a.s.l.).

2.3.6 Meteorological forcing ensemble

Applying the adjustments in temperature (Section 2.3.4) and in solid precipitation (Section 2.3.5) to the SAFRAN data led to the adjusted forcing. From this, we built an ensemble of forcings with 40 members (Cluzet et al., 2020). This ensemble of forcings
260 allowed us to take into account the meteorological uncertainties which generally prevail on the snow model uncertainties in the case of snowpack simulations (Raleigh et al., 2015; Günther et al., 2019). This also enabled us to estimate the meteorological uncertainties on the simulation results.

Five meteorological variables were perturbed (air temperature T , incoming direct shortwave radiation SW_{dir} , incoming long-wave radiation LW , wind speed W and solid precipitations SP) using a first-order autoregressive model $AR(1)$. The stochastic
265 perturbation method was inspired from Charrois et al. (2016); Cluzet et al. (2020), and detailed in Appendix C1. For a given member, the same perturbations were spatially applied to all simulation points. Each variable was perturbed independently from other variables. For each variable, the perturbation term X_t depends on a decorrelation time τ and an amplitude σ_X^2 . The exact relationship is explained in detail in Appendix C1. Given an additive variable V_t (T or LW) at time-step t , the perturbed variable V_t^* is defined as $V_t^* = V_t + X_t$, and in case the variable is multiplicative (SW or W), V_t^* is defined as $V_t^* = V_t \cdot (1 + X_t)$.
270 We applied the perturbations on a daily scale with a decorrelation time $\tau = 24$ h for T , SW_{dir} , LW and W , and on a season scale with $\tau_{SP} = 1500\text{h} = 62.5$ days for solid precipitations. For each variable, the amplitude σ_X^2 of the meteorological uncertainties were induced by the standard deviation of the difference between the observed variable (at moraine AWS, Section 2.3.2) and the SAFRAN variable (interpolated at the location of the moraine AWS) over the period 01/01/2015-30/09/2022. For each variable, this standard deviation was $\sigma_X = 1.43$ °C for T , $\sigma_X = 28.0$ W m^{-2} for LW , $\sigma_X = 142$ W m^{-2} for SW , $\sigma_X = 2.08$
275 m s^{-1} for W . For solid precipitations, we used the standard deviation between the modelled winter SMB (with the correction of solid precipitations of Section 2.3.5) and the observed winter SMB, for all measurements between 2,300 and 2,400 m a.s.l. over the period 2018-2022. This led to $\sigma_X = 0.36$ m w.e.

2.4 Surface mass balance model

For each simulation point and associated forcing inputs described in Section 2.3, we performed independent simulations of
280 SMB at 250 m horizontal resolution (Fig. 1d). The 250 m horizontal resolution was chosen as a trade-off between simulation costs and model performances, which generally drops at 500 m resolution in mountainous area, *e.g.*, Baba et al. (2019). We used the detailed snowpack model SURFEX/ISBA-Crocus (Vionnet et al., 2012), which was already used to simulate glacier SMB regardless of the glacier size, *e.g.*, Gerbaux et al. (2005); Lejeune et al. (2007); Dumont et al. (2012); Réveillet et al. (2018). Crocus simulates the evolution of the snow cover with a 15 minute time-step representing different processes including

285 thermal diffusion, phase change, water flow, snow metamorphism and compaction. Snow optical properties (single scattering albedo and absorption cross section for each snow layer) are calculated from the prognostic variables of the model (grain size, density, layer thickness). In Crocus, the snowpack is discretized as a one dimensional column with up to 50 layers, each of them having its own snow/ice properties. This layering is determined by an ensemble of rules described in Vionnet et al. (2012). An initial state of the glacier was prescribed at each simulation point, with a vertical column of several ice layers with a density
 290 of 917 kg m^{-3} as in Vionnet et al. (2019). The resulting height of the total column was initially set to an arbitrary value of 100 m w.e., with a temperature of $0 \text{ }^\circ\text{C}$. The roughness length of snow z_0 was set to 0.5 mm, and the roughness length of ice was set to $2 \times z_0$. These values were selected to obtain turbulent fluxes consistent with the measurements at the glacier AWS. This ratio between snow and ice roughness length was kept constant for the entire study. These values of roughness length were inside the usual ranges described in Cuffey, Paterson (2010). Ice albedo of 0.23 was inferred from S2 images (Section
 295 2.2.5). Given the substantial influence of parametrization choices for albedo and roughness values on SMB (*e.g.*, Réveillet et al., 2018), the sensitivity to these parameters was analyzed in Section 3.3.

We collected Crocus outputs every 6 hours for all simulation points (total snow water equivalent (m w.e.), and broadband albedo). We also computed the mean density (kg m^{-3}) in the top 5 cm of the simulation, named in this study top density. This fixed height allows us to be independent of the numerical discretization. We also derived the simulated surface type from the
 300 top density: ice if top density is higher than 850 kg m^{-3} (Cuffey, Paterson, 2010), else snow. The mean simulated snowline elevation was computed at simulation horizontal resolution (*i.e.*, 250 m) using the same method as for the S2 images (Section 2.2.2) and was therefore compared to the mean observed snowline elevation from S2 images in Section 3.1. This allows us to evaluate the snowpack melt-out date.

2.4.1 LAP implementation

305 Since Tuzet et al. (2017), a parametrization allows Crocus to explicitly model the interactions between LAPs and snow. This parametrization was used in this study. Each snow layer contains a mass of each type of LAPs which enables to compute the spectral albedo of the snow surface at 20 nm resolution accounting for LAPs using the model Two-streAm Radiative TransfEr in Snow (TARTES, G. Picard, Q. Libois, 2024). To this end, TARTES computes the light penetration and energy absorption using snow properties and the LAPs mass in each layer. In this study, we used two types of LAPs, mineral dust and BC. To
 310 compute the albedo of snow, the refractive indices of ice was set as in Réveillet et al. (2022). Particularly, the mass absorption efficiency of dust $\text{MAE}_{\text{dust}}(\lambda)$ used for this study was the MAE of the Lybian dust from Caponi et al. (2017), *i.e.*, $\text{MAE}_{\text{dust}}(\lambda) = \text{MAE}_{\text{dust}}(\lambda_0) \times \left(\frac{\lambda}{\lambda_0}\right)^{-\text{AAE}_{\text{dust}}}$ where $\lambda_0 = 400 \text{ nm}$, $\text{MAE}_{\text{dust}}(\lambda_0) = 71 \times 10^{-3} \text{ m}^2 \text{ g}^{-1}$, and the Ångström absorption exponent $\text{AAE}_{\text{dust}} = 3.2$. The MAE of BC at 550 nm used for this study was $7.5 \text{ m}^2 \text{ g}^{-1}$ (Bond, Bergstrom, 2006). To quantify the impact of dust, BC needed to be taken into account since the impact of dust relies on BC concentration in the snowpack. This
 315 is discussed in Section 4.2. For the two uncertainty tests on the dust MAE (Fig. 8), we used the highest and the lowest values of dust MAE considering the regions of Sahel and Sahara of Caponi et al. (2017), respectively [$\text{MAE}_{\text{dust}}(\lambda_0) = 27 \times 10^{-3} \text{ m}^2 \text{ g}^{-1}$, $\text{AAE}_{\text{dust}} = 3.3$] and [$\text{MAE}_{\text{dust}}(\lambda_0) = 630 \times 10^{-3} \text{ m}^2 \text{ g}^{-1}$, $\text{AAE}_{\text{dust}} = 3.4$].

The implementation of Tuzet et al. (2017) allows impurities to percolate with liquid water from one layer to the underlying one and prevent the complete accumulation of LAPs at the very top of the snowpack during melt. In Crocus, this process is parameterized for each LAP type with a scavenging efficiency. For large LAPs such as mineral dust, with a typical radius of 5 microns, Conway et al. (1996) explained that these particles stay near the snow surface, almost not percolating with liquid water, hence we set dust scavenging coefficient $k_{\text{dust}} = 0$. For BC, the reference scavenging efficiency k_{BC} used by previous studies is 0.2 (e.g., Flanner et al., 2007; Gabbi et al., 2015), then we also chose this value as reference. Sensitivities to both scavenging efficiencies were presented in Section 3.3 and discussed in Section 4.2.

325 **2.4.2 Model modifications**

Since the Crocus model was primarily developed for avalanche forecasting, the layering rules discourage the merging of layers with different snow grain properties, e.g., most of the time a faceted crystal layer would not be merged with a rounded-grains layer, and a snow layer would not be merged with an ice layer. However, those initial layering rules allowed the merging of layer containing very different LAPs concentration if their microstructure properties were sufficiently close. When it occurred several times, especially with thick layers, this numerical process could artificially redistribute impurities across the entire snowpack. This spurious redistribution of LAPs, which modified their reappearance date during the melt period and their impact on albedo had to be avoided. Hence, we added a new merging discretization rule that prioritized the conservation of layers with high dust concentration. We chose to prioritize mineral dust because its concentration in seasonal snow is vertically more discontinuous than that of BC. However, layers containing a high concentration of both mineral dust and BC, e.g., top of the firn from the previous year, were preserved through the prioritization of layers with a high concentration of dust.

Two other modifications were implemented in the model. First, as the concentrations of mineral dust and BC in the ice were unknown, the TARTES radiative scheme was not used in case ice was at the top of the snowpack. The model considered ice at the top of the snowpack if the top density was higher than 850 kg m^{-3} which is close to the pore close-off density, and in this case, the albedo was set to a constant value inferred from Section 2.2.5. Hence, we did not model the difference in ice albedo between simulations with and without impurities. Second, we implemented an option to disable the effect of one LAP type on the spectral snow albedo. More precisely, the discretization rules stayed the same as in the reference version but the LAP acted as transparent in the radiative transfer model TARTES. This feature was used to quantify the impact of mineral dust and BC in Section 3.2.

2.5 Description of the simulation setup and metrics

345 All simulations included two phases: (i) the spin-up (2008-2018); (ii) the period of interest (2019-2022). The chronology and the use of the different data are summarized in Appendix Fig. A1. Initially, a column of temperate ice was prescribed for all simulations (Section 2.4), and the spin-up aimed to initialize the LAPs contents in old firn in the accumulation area and to reach a thermal equilibrium of deep ice layers.

The forcing ensemble was used as input to the simulation model to get the simulations considering the impact of mineral dust (simulations named "dust"), and the simulations without the impact of mineral dust (simulations named "no-dust"). Simulations

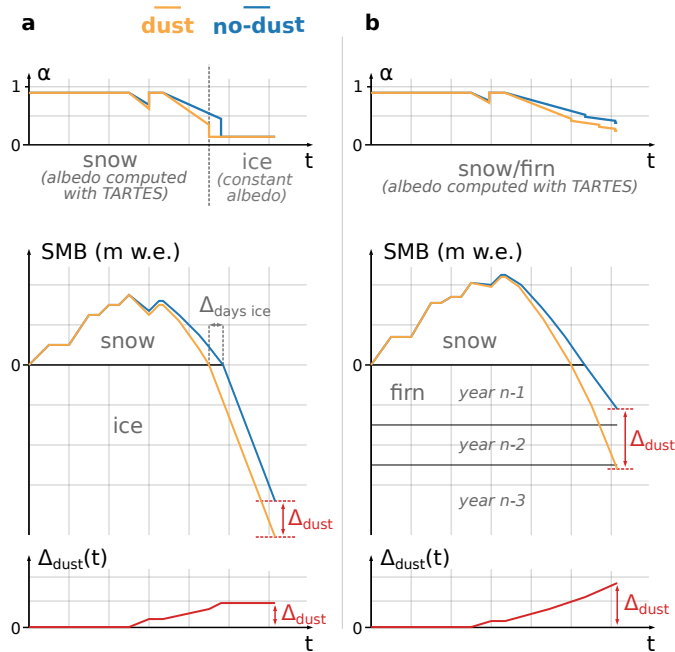


Figure 2. Possible evolution of the albedo, SMB and dust impact Δ_{dust} , over one year, with and without dust, for (a) a location in the ablation area where snow accumulated on ice during winter, and (b) a location in the accumulation area where snow accumulated on top of the firn from previous years.

without the impact of dust were obtained without the radiative effect of dust as explained in Section 2.4.2. As a result, we obtained 40 paired simulations (dust and no-dust). An important point is that BC remained present in all simulations. An alternative could have been to use the difference between (i) the simulation with dust and without BC, and (ii) the simulation without LAP at all as in Réveillet et al. (2022). This would have likely lead to larger quantified impacts (Flanner et al., 2012).
 355 However, we chose the simulation with both BC and dust as the reference as it is closer to the observed state of the snowpack, hence avoiding an overestimation of the dust impact and staying in line with other studies, *e.g.*, Flanner et al. (2007, 2012)). A fictive example of evolution of the glacier state with a single pair of the ensemble is presented in Figure 2. This illustration reminds that the impact of dust was only taken into account in snow and firn, not in ice. However, in the ablation area, by advancing the snow melt-out date, simulations with LAPs expose the ice earlier than simulations without LAPs. Since the
 360 albedo of ice is lower than the albedo of snow, ice acts as a positive feedback for melt and leads to a lower summer surface mass balance. To quantify this feedback, we had to simulate both snow and ice. In the same way, Réveillet et al. (2018) showed that lower winter snow accumulation led to higher summer melt due to this feedback.

We evaluated the SMB of the period of interest in Section 3.1. We analyzed the results during this period by comparing the years 2019-2021 to the year 2022 at each simulation point and at the glacier-scale (Section 3.2). To do so, we used the
 365 following metrics. The dust impact Δ_{dust} (m w.e.) was computed as the difference in annual SMB between dust and no-dust

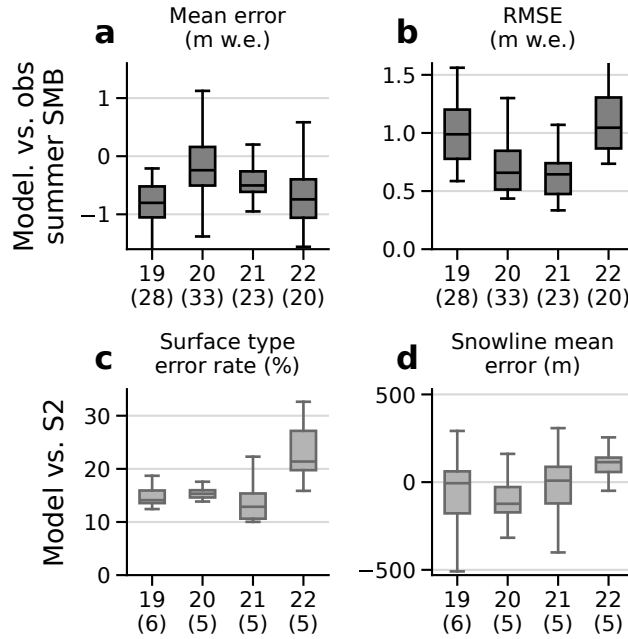


Figure 3. (a) Mean error between point measurements and modelled summer SMB for the summers 2019 to 2022 for the 40 members of the ensemble using q point measurements (in parenthesis). (b) Same as panel (a) with root mean square error. (c) Surface type error rate between Sentinel-2 and simulated surface type using p S2 images (in parenthesis) for the years 2019 to 2022. (d) Snowline mean elevation error between S2 and simulated snowlines using p S2 images for the years 2019 to 2022. All boxes in the figure show the quartiles of the distributions. The upper bound for the upper whiskers extends to a last value less than $Q3 + 1.5 \times (Q3 - Q1)$, and the lower bound for the lower whiskers extends to a first value greater than $Q1 - 1.5 \times (Q3 - Q1)$.

simulations. The melt fraction due to dust Δ_{dust}/M (m w.e. / m w.e.) was computed as the ratio between the dust impact Δ_{dust} and the total melt of snow and ice of the year in the simulation taking dust into account. The number of days with ice at the top of the simulation was called $N_{\text{ice-days}}$. The time duration during which ice was exposed in the simulation with dust and not exposed in the simulation without dust was computed as $\Delta_{\text{ice-days}} = N_{\text{ice-days}}^{\text{dust}} - N_{\text{ice-days}}^{\text{no-dust}}$. To find results at the glacier scale, we first averaged the values of all simulation points, and we then computed the median and Q10-Q90 of these averages at the glacier scale.

Outside of the ensemble framework, we also ran different simulations using the adjusted forcing and the reference model parametrization in which we modified either an input or a model parameter. This led to the sensitivity analysis of Section 3.3.

3 Results

375 3.1 Evaluation of the simulated SMB

Figure 3 illustrates the evaluation of the simulated annual SMB for the hydrological years 2019 to 2022. For each year, we computed the mean error and the root mean square error (RMSE) for all the simulated summer SMB against the point measurement of summer SMB (Fig. 3a,b), supported by 28, 33, 23 and 20 stake measurements, respectively. The spread of the ensemble included the zero mean error for the year 2020, 2021 and 2022. For all years, the summer simulated SMB were
380 lower than the observations. Moreover, for each year, some members had a RMSE lower than 1 m w.e. against the summer point measurements. If we only consider the observed summer SMB under and above 2,800 m a.s.l. (respectively 84 and 20 measurements), some members still had a RMSE lower than 1 m w.e. These errors can be compared to the total melt of snow and ice during the summer period, that is typically 5-9 m w.e. in the ablation area, 2-4 m w.e. near the snowline elevation, and 0-2 m w.e. in the accumulation area.

385 Then, we compared our simulations against S2 images. For the years 2019 to 2022, all members exhibit a surface type error rate between 8 and 35 % computed over more than five S2 images per year. In addition, for each year, the zero mean snowline error was always within the spread of the ensemble. The evaluation of the no-dust simulations are presented using the observed summer measurements and the S2 images in Appendix Fig. D1.

Last, we compared the mean annual simulated SMB from 08/09/2018 to 05/10/2022 with distributed annual SMB derived
390 from Pléiades elevation change and velocity fields, called here Pléiades SMB. Figure 4 shows that the distributed Pléiades SMB had higher extreme values (-15.2 to 8.6 m w.e. yr⁻¹) than the simulated SMB (-5.8 to 1.1 m w.e. yr⁻¹) and a higher variance with standard deviation of distributed SMB $\sigma_{Pléiades} = 3.3$ m w.e. yr⁻¹ and $\sigma_{simu} = 1.8$ m w.e. yr⁻¹. The glacier-wide Pléiades SMB was -0.7 m w.e. yr⁻¹, and the simulated SMB was -1.9 m w.e. yr⁻¹. For most of the simulation points (129, black points in Fig. 4), the Pléiades and simulated SMB uncertainties intersected. For a minority of points (31, red points
395 in Fig. 4), Pleiades SMB uncertainties did not match the simulated SMB uncertainties. Most of those points were located on the southern part of the glacier, in the accumulation area, at the base of steep north-facing headwalls, where several Pléiades SMB points were higher than 3 m w.e. yr⁻¹ while the simulated SMB did not exceed 2 m w.e. yr⁻¹. This difference is likely due to avalanches and discussed in Section 4.3.

3.2 Simulated impact of dust

400 3.2.1 At the local scale in different sectors of the glacier

Figure 5 shows the evolution of the snow water equivalent relative to the 1st October for four hydrological years, from 2019 to 2022, at three different locations using the ensemble of simulations. Point P1 is in the ablation area, at around 2,400 m a.s.l. Point P2 is in the accumulation area, above the end-of-summer snowline of 2021 but under the end-of-summer snowline of 2022, at around 2,900 m a.s.l. Point P3 is in the accumulation area at around 3,500 m a.s.l. (see exact locations in Fig 1d).

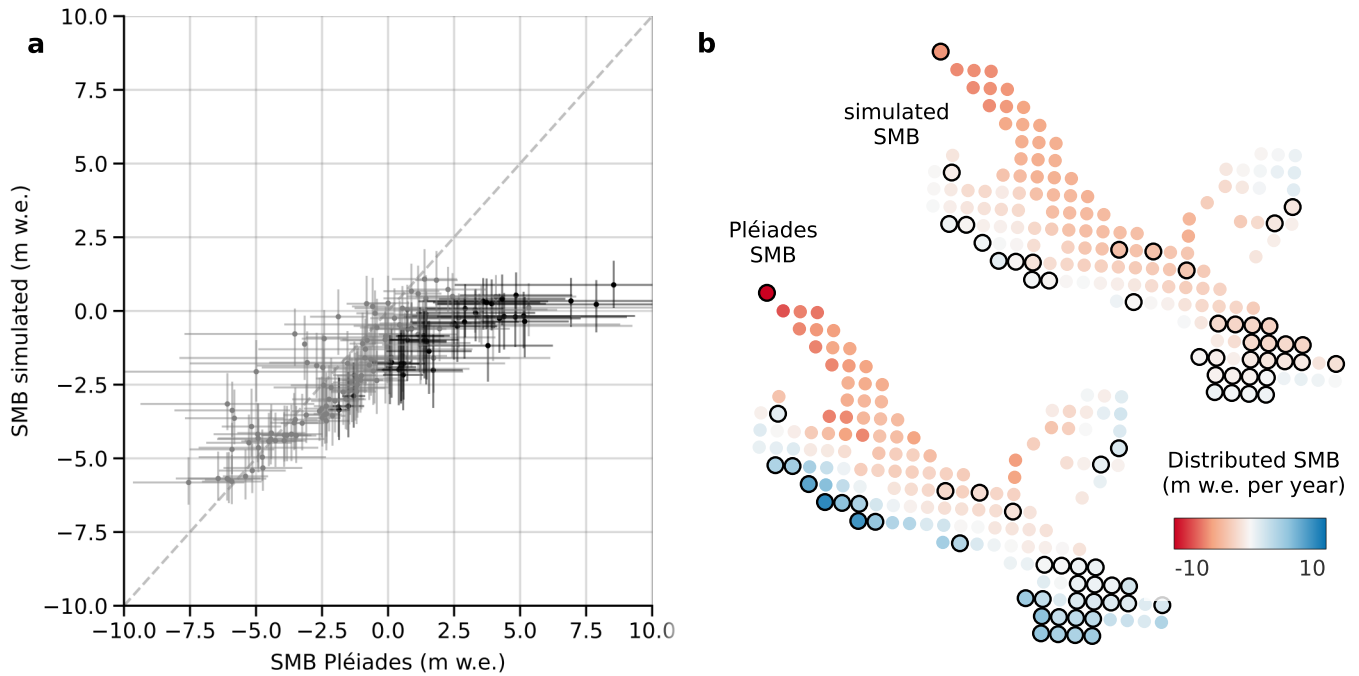


Figure 4. (a) Scatter plot of mean annual SMB inverted from Pléiades data vs. simulated SMB, over the period 08/09/2018 to 05/10/2022. Median-Q10-Q90 are represented for simulations, mean and a 2-standard deviations from the mean are represented for the Pléiades SMB. Points with uncertainty that do not cross the 1:1 line are plotted in black, the others in gray. (b) Distributed Pléiades and simulated SMB (medians). Points plotted in black in panel (a) are encircled in black.

405 At point P1 in the ablation area, the annual simulated SMB was negative for all years from 2019 to 2022 (orange curve in Fig 5). Without mineral dust, the simulated annual SMB was still largely negative (blue curve in Fig. 5). The difference in annual SMB for the simulations with and without dust in snow Δ_{dust} remained below 0.6 m w.e. for all years. The fraction of melt due to dust Δ_{dust}/M was less than 10 %. The number of days with ice at the surface was between 60 and 140 days depending on the year, and the difference of time with ice exposed at the surface taking into account or not the impact of dust

410 was lower than 10 days. At point P3, at the top of the accumulation area, the simulated annual SMB was positive for all years except 2022. At this point, the impact of mineral dust accounted for less than 0.3 m w.e. for each year in the period 2019-2021, and for less than 0.9 m w.e. in 2022. It represented between 0 and 25 % of the total melt. Ice was never exposed at this point. At point P2, near the end-of-summer snowline, the simulated annual SMB was either positive (2020, 2021) or negative (2019, 2022). This allowed, or not, the formation of a firm layer depending on the year. For years 2019, 2020 and 2021, the dust impact

415 at P2 ranged from 0.25 to 0.75 m w.e. For 2022, the dust impact was 1.15 m w.e. [0.90, 1.34] (median, Q10-Q90), which represent 24.6 % [19.1, 27.3] of the total melt. In 2022, ice was exposed during 42 days in the simulation that takes dust into account.

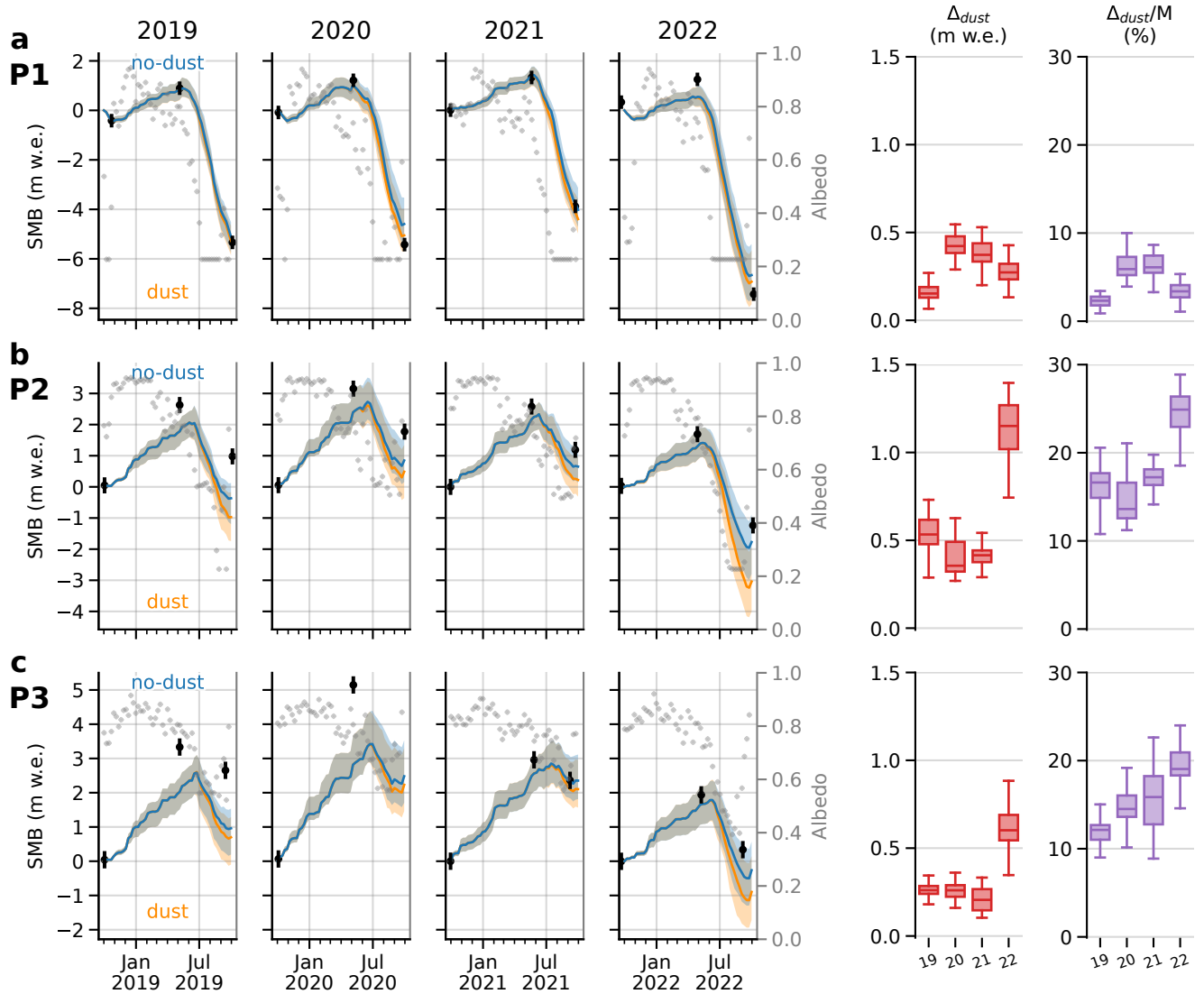


Figure 5. SMB evolution and albedo (dots) at noon for hydrological years 2019 to 2022 at three different locations. Median (solid line) and Q10-Q90 of the 40 ensemble members for dust and no-dust simulations. Black points and lines are the observed SMB and their uncertainty using the nearest measurement point. Δ_{dust} (m w.e.) is the difference in SMB between the simulation with and without mineral dust, and Δ_{dust}/M (%) is the ratio between Δ_{dust} and the total melt. P1 was in the ablation area (2,400 m a.s.l.), P2 near the equilibrium-line elevation (2,900 m a.s.l.) and P3 in the accumulation area (3,500 m a.s.l.), see Fig. 1d for precise locations. SMB scale is different at each location. Double digits refers to the years.

The spread of the ensemble for the dust impact varied depending on the location and the year. For instance, there was a small ensemble spread in dust impacts Δ_{dust} , *e.g.*, at P1 with all Δ_{dust} ranging within ± 0.3 m w.e. for each year, compared to P2 with

420 a higher ensemble spread, *e.g.*, with Δ_{dust} ranging between 0.75 and 1.4 m w.e. in 2022. However, this spread of dust impact is always lower than the spread of annual SMB induced by the meteorological ensemble, that is always larger than 1 m w.e. For the three points, we observed that the impact of dust was mainly effective during the summer. Indeed, for both simulations with and without dust, their winter accumulations in Fig. 5 were very similar, while the ensemble means of SMB gradually diverge during the summer melt.

425 3.2.2 At the glacier scale

At the glacier scale, the simulated dust impact on the annual SMB was higher in 2022 than in previous years, in agreement with results at the three locations P1, P2 and P3. For years 2019 to 2021, the median [Q10-Q90] of the annual SMB decrease due to dust at the glacier scale were 0.31 m w.e. [0.29, 0.35], 0.42 m w.e. [0.39, 0.47], and 0.45 m w.e. [0.41, 0.49], respectively, representing 9.1 % [8.3, 9.9], 12.5 % [11.8, 13.2], 14.8 % [13.4, 16.1] of the total annual melt. However, in 2022, the impact
430 due to dust in snow and firn rose to 0.63 m w.e. [0.54, 0.69] representing 13.2 % [11.8, 14.7] of the total melt. In 2022, the albedo averaged over the whole glacier at noon over the year decreased by 0.03 [0.028, 0.033] due to dust. When restricted to summer 2022, from May to September, snow albedo decreased by 0.062 [0.056, 0.067].

Overall, when looking at each point simulation, we found very different dust impacts over the glacier depending on the location, from almost 0 m w.e. to above 1 m w.e., due to very different impact of dust on snow summer albedo (summer albedo
435 decreased from 0 to 0.12 depending on the location, see Appendix Fig. E2). When comparing each year, for all simulation points, the dust impacts from year 2019 to 2021 were mostly lower than that of 2022 in the accumulation area (Appendix Fig. E1).

Thereafter, we focus on the year 2022, as it presents the highest dust impacts. However, the values for the complete period 2019-2022 are presented in Appendix Fig. E1, E2 and E3. Figure 6 illustrates the spatial distribution of the simulated dust
440 impacts in 2022. The dust impact presented a high spatial variability, ranging from 0 to 1.2 m w.e., was lower below the end-of-summer snowline of 2021 and in the upper part of the accumulation area. Although the dust impact values in 2022 at higher elevations were close to the value at lower elevations (Δ_{dust} between 0.2 and 0.6 m w.e.), the melt fraction at higher elevations was much higher ($\Delta_{\text{dust}}/M > 15\%$ at high elevation *vs.* $\Delta_{\text{dust}}/M < 5\%$ at lower elevations). In 2022, the highest impact of dust occurred around 3,000 m a.s.l., which was just above the end-of-summer snowline of 2021 (Fig. 1a), and differed depending
445 on the aspect: at 3,000-3,200 m a.s.l. for the north-eastern part of the glacier which is south-west facing, at 2,900-3,100 m a.s.l. for the top of the main tongue which is north facing, at 2,900-3,100 m a.s.l. for the western part of the glacier which is north-east facing.

The spatial pattern of the albedo reduction due to dust is similar to the spatial pattern of the dust impact (Fig. 6c and d), with a summer albedo decrease that is nearly the double of the annual albedo decrease. At the bottom of the main glacier tongue,
450 numerous simulation points had ice exposed at the surface for more than 100 days in 2022 (Fig. 6e). Almost all points below the 2021 end-of-summer snowline had ice at the surface for more than two months. The points with the longer time duration with ice at the surface in the dust simulation, but snow/firn in the no-dust simulation, were located near the end-of-season

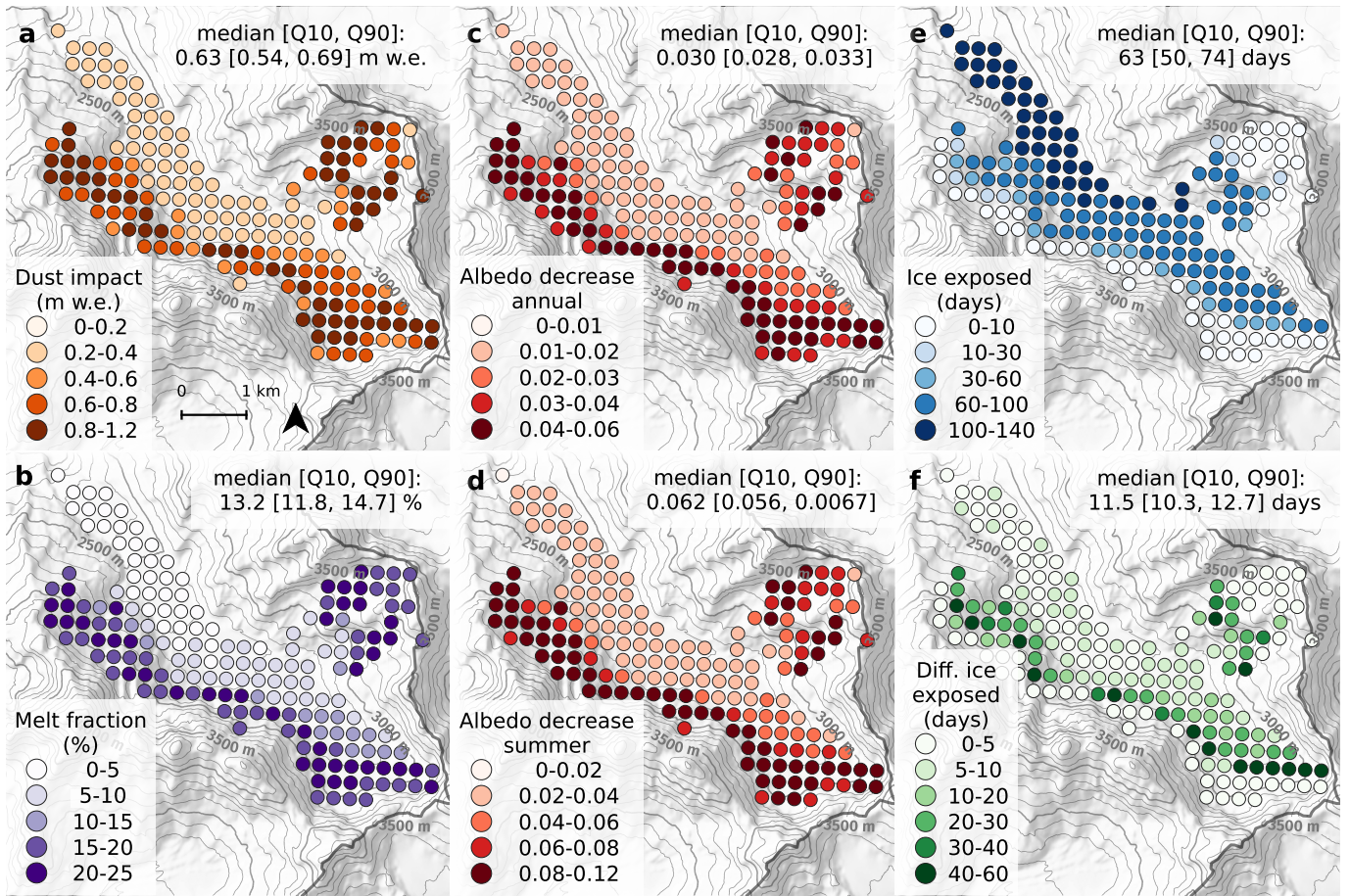


Figure 6. At each simulation point for hydrological year 2022 (01/10/2021 to 30/09/2022): (a) Dust impact Δ_{dust} , *i.e.*, difference in simulated SMB for dust and no-dust. (b) Melt fraction Δ_{dust}/M , *i.e.*, fraction of the melt due to dust. (c) Annual albedo decrease due to dust. (d) Summer albedo decrease due to dust. (e) Number of days with ice exposed at the surface for the dust simulation. (f) Number of days with ice exposed for the dust simulation, but not for the no-dust simulations. The colors represent the median of the ensemble at each point. The aggregated value refers to the median and [Q10-Q90] range (over the 40 members) of the mean over all simulation points. Background map from MapTiler.

snowline of 2021 (Fig. 6e) with up to 40-50 days of difference. At the bottom of the main tongue, this time duration dropped to less than five days difference.

455 3.3 Sensitivity analysis

We investigated the sensitivity of the principal inputs and model parameters to understand how different values of our inputs and model parameters can affect the results. We investigated the impact of ice albedo modifications ($\pm 20\%$), roughness length ($\pm 20\%$), BC scavenging efficiencies ($\pm 20\%$), mineral dust scavenging efficiency (0.04 and 0.2 instead of 0), dust and BC

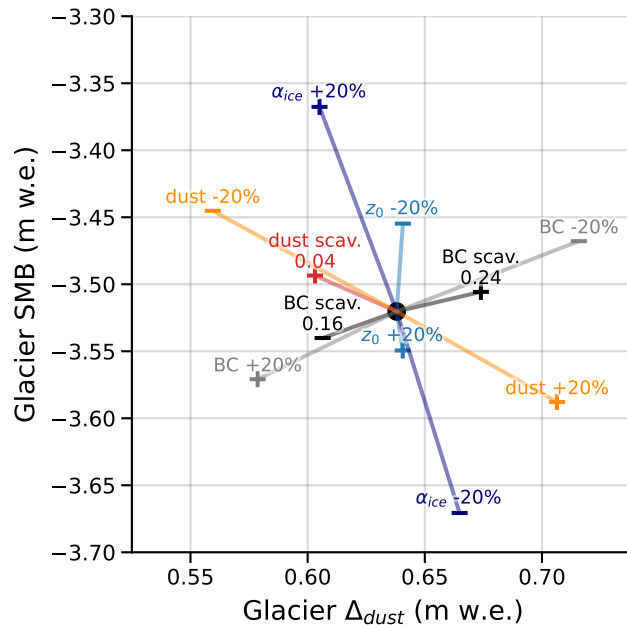


Figure 7. Sensitivity of glacier-wide annual SMB (y-axis) and dust impact Δ_{dust} (x-axis) to forcing inputs and model parameters relative to the reference simulation (central black dot) for hydrological year 2022.

deposition fluxes ($\pm 20\%$). Figure 7 shows the difference caused by these modifications on: (i) the annual glacier SMB; and (ii) the estimated dust impact Δ_{dust} at the glacier scale in 2022. Increasing (decreasing) ice albedo by 20% increased (decreased) the annual glacier SMB by around 0.14 m w.e. For the roughness length, an increase (decrease) of 20% increased (decreased) the annual glacier SMB by around 0.03-0.08 m w.e. Modifications on ice albedo or roughness length modified the dust impact by less than 0.04 m w.e. An increase (decrease) in dust and BC input fluxes lowered (increased) the annual glacier SMB by around 0.05 m w.e., hence the model has the same sensitivity to both LAP deposition fluxes. Moreover, increasing (decreasing) dust input fluxes increased (decreased) the dust impact by 0.08 m w.e. An increase in scavenging efficiencies, which lowers the impurity accumulation at the snow surface, increased the annual glacier SMB. Overall, these results showed that the sensitivity of the dust impact to dust or BC deposition fluxes was larger than the sensitivity to their respective scavenging coefficients and to other parameters of the model such as the ice albedo and the roughness length. We finally observed that the glacier SMB and dust impacts resulting from the sensitivity tests described previously were included in the ensemble spread (see Fig. 8), hence included in the meteorological uncertainty. Specifically, for glacier SMB, the meteorological uncertainty was much wider than the spread of all the sensitivity tests described above, whereas for glacier dust impact, the meteorological uncertainty was a bit larger than a variation of $\pm 20\%$ of dust inputs. Nevertheless, these sensitivities do not represent the impact of the uncertainties of each input and parameter, that are later discussed in Section 4.

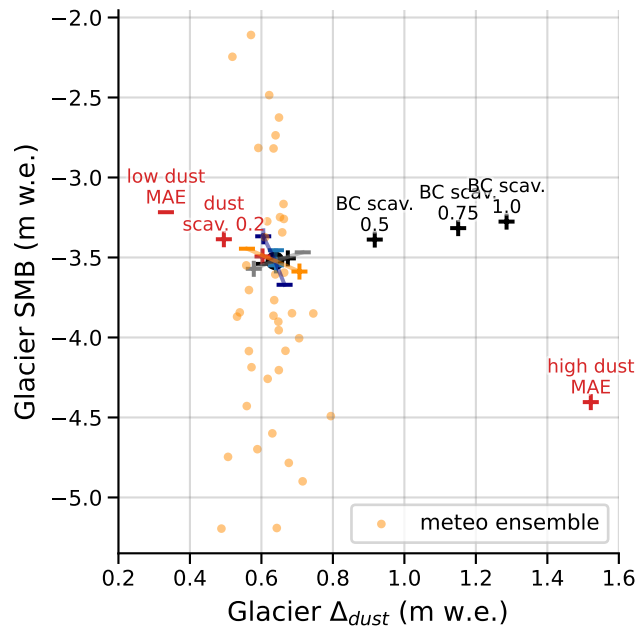


Figure 8. Impact of uncertainties relative to LAP scavenging efficiencies and deposition fluxes on the glacier-wide annual SMB (y-axis) and dust impact Δ_{dust} (x-axis) for hydrological year 2022. Reference simulation is represented by the central black dot. The 40 members of the ensemble are represented with the orange dots.

In addition to this sensitivity analysis, and as the scavenging efficiency of BC is subject to large uncertainties (Section 4.2), we also tested much higher BC scavenging efficiencies k_{BC} of 0.5, 0.75 and 1.0 (Fig. 8). These BC scavenging efficiencies slightly lowered the annual glacier SMB by 0.15 to 0.30 m w.e. compared to the previous efficiencies. However, such BC scavenging efficiencies increased the impact of dust up to 1.3 m w.e. in the annual glacier SMB of 2022 compared to 0.63 m w.e. with the initial BC scavenging efficiency of 0.2. A dust impact of 1.3 m w.e. represented approximately 25 % of the total melt. Figure 8 shows that the sensitivity of the dust impact to BC scavenging efficiency is not linear. The growing impact of mineral dust with increasing BC scavenging efficiency is discussed in Section 4.2.

4 Discussion

In this study, we simulated the SMB of Argentière Glacier for four years with an advanced snow model that explicitly takes into account the impact of mineral dust and BC. At the glacier-wide scale, we showed that mineral dust lowered the annual SMB by up to 0.63 m w.e. [0.54, 0.69] in 2022, which represents 13 % [12, 15] of the total melt. At the point scale in specific areas of the glacier, the impact of mineral dust lowered the annual SMB up to 1.2 m w.e.

4.1 Role of dust

If the impact of mineral dust strongly varied with the location at the glacier surface, its deposition flux was homogeneous across the whole glacier. The results shown in figure 5 illustrate three different cases.

The first case corresponds to the ablation area where the annual SMB and the mean annual albedo with dust were lowered
490 by 0-0.5 m w.e. and 0-0.02, respectively (Fig. 2a). Since we only simulated the impact of dust inside snow, and not on ice, two reasons explain these differences in SMB and albedo at lower elevation: (i) mineral dust lowers the albedo of the seasonal snow; and (ii) ice, which has a lower albedo than snow, is exposed earlier during the melt season, and acts as a positive feedback on melt. If we had also modelled the impact of dust on the ice surface, the dust impact in the ablation area would have likely been higher.

495 The second case corresponds to the accumulation area, where snow was always present at the glacier surface, and both annual SMB and albedo were lowered by 0.2-0.8 m w.e. and 0.02-0.04, respectively. In this case, snow from the winter does not completely melt, dust stays exposed at the surface during a long time period and leads to a higher melt fraction than at low elevation.

The third case corresponds to the area just above the end-of-summer snowline from previous years, when atmospheric
500 conditions during the summer period lead to a negative annual SMB. In such a case, the firn layers from the previous years with accumulations of LAPs reappear at the surface, leading dust to lower the annual SMB and albedo by 0.8-1.2 m w.e. and 0.03-0.05, respectively. For instance at point P2, for most of the members the annual SMB was positive in 2020 and 2021, allowing the re-exposure of the accumulated LAPs in 2022, when the annual SMB was negative. This is also the scenario of Fig. 2b. This persistent impact of LAP over several years has already been mentioned by Gabbi et al. (2015) in the European
505 Alps, and more recently by Möller et al. (2019) in Iceland. In such a scenario, we noted that the spread of dust impacts induced by the ensemble was larger, and this could be generalized to nearly all points above the end-of-summer snowline of 2021 (Appendix Fig. E1). This higher ensemble spread might be due to: (i) a longer exposition of dust at the snow surface, with different shortwave radiation conditions depending on the ensemble member; (ii) a larger diversity of scenarios, with ice exposed during the summer for some members, and only firn exposed for other members. To sum up, mineral dust has varying
510 impacts and uncertainty depending on the location on the glacier and the time of the year, with a maximum impact of dust found close to the end-of-summer snowline. Such an impact variability could only be found using a fine horizontal spatial resolution, here 250 m.

At the glacier scale, our results for Argentière Glacier showed that the impact of dust on the glacier-wide annual SMB ranges between 0.31 and 0.63 m w.e. (medians) for the years 2019 to 2022, which was an order of magnitude higher than
515 the mean annual dust impact of 0.03-0.06 m w.e. computed at two points over a century on Clariden Glacier by Gabbi et al. (2015). Such a difference may be explained by multiple factors. First, both studies focused on different time periods. Thus, the LAP deposition flux sources, which highly vary with time, were also different. For instance, the annual dust deposition fluxes present a high inter-annual variability (*e.g.*, Di Mauro et al., 2015; Réveillet et al., 2022), and the annual BC deposition fluxes significantly decreased after the 1990s in the French Alps (*e.g.*, Sun et al., 2020; Grange et al., 2020; Réveillet et al., 2022),

520 which could explain a lower impact of BC and a higher impact of dust in the 21th century. Second, both studies focused on different geographic locations. Clariden Glacier is located in the northern part of the European Alps, that is less exposed to Saharan dust depositions. For instance, Dumont et al. (2023) showed that the deposited dust mass decreased with the distance to the source during a single Saharan dust deposition event, with less dust deposited in the Swiss Alps compared to the French Alps. Ultimately, the mass absorption efficiencies (MAE) of both studies were different. For BC, Gabbi et al. (2015) used a
525 constant $\text{MAE}_{\text{BC}} = 6.8 \text{ m}^2 \text{ g}^{-1}$, while for our simulations, we used a higher MAE_{BC} depending on the wavelength λ such as $\text{MAE}_{\text{BC}}(\lambda) = 7.5 \text{ m}^2 \text{ g}^{-1}$, at 550 nm. We could not directly compare the MAE of dust, since Gabbi et al. (2015) used a MAE of Fe-oxides and we used a MAE of mineral dust. However, we computed the broadband ratio $(\text{MAE}_{\text{BC}} \times m_{\text{BC}}) \div (\text{MAE}_{\text{dust}} \times m_{\text{dust}})$ with m_{LAP} the mean annual deposited mass of each LAP. For Gabbi et al. (2015), this ratio was close to 10, *i.e.*, BC has potentially more impact than dust. This is in line with their results showing that the reduction of the SMB by BC is an order of
530 magnitude higher than that of dust. For our study, this ratio was close to 1, *i.e.*, dust and BC have potentially the same impact in case no scavenging is taken into account. Besides other model and input differences, this could partially explain that the dust impact of this study is higher than that of Gabbi et al. (2015) by an order of magnitude.

The range of uncertainty was inferred by a meteorological ensemble, and in 2022, the obtained range was [0.54, 0.69] m w.e. When varying the dust deposition flux by $\pm 20 \%$, the resulting uncertainty is included in the previous range. We found
535 a spatial variability of $2\sigma \approx 45 \%$ on the dust deposition fluxes around the selected point of the ALADIN grid 2.3, that the meteorological ensemble does not take into account. However, the impact of the dust deposition uncertainty has likely the same order of magnitude than the impact of the meteorological uncertainty (≈ 0.1 m w.e. in 2022).

The dust scavenging efficiency k_{dust} that was set to 0 in the reference version, *i.e.*, no scavenging of dust (see Method Section 2.4.1). A higher $k_{\text{dust}} = 0.04$ led to a lower impact of dust (Fig. 7). Although this was poorly documented in the
540 existing literature, we suspected that dust scavenging efficiency at the snow surface could be significantly higher than the previous sensitivity test. So we added a test of uncertainty using $k_{\text{dust}} = 0.2 = k_{\text{BC}}$ (Fig. 8), which is likely too high since BC particles scavenge more easily than large particles such as dust (*e.g.*, Conway et al. (1996); Doherty et al. (2013)). The dust impacts using those two dust scavenging efficiencies were still inside the uncertainty induced by the meteorological ensemble.

The MAE of dust used in this study was slightly lower than initial values used in previous studies in the framework of a seasonal alpine snowpack at intermediate elevations (Tuzet et al., 2020; Réveillet et al., 2022). The reliability of this parametrization was assessed by the evaluations of section 3.1 and the evaluation of the modelled snow albedo in Appendix Fig. B3. Such lower MAE implicitly accounts for the probable aggregation of LAP (likely due their high concentrations during long melt seasons) that lowers the MAE (*e.g.*, Bond, Bergstrom (2006); Schwarz et al. (2013)). In addition, the temporal variability of the absorption efficiency of dust was not represented in the model: the MAE used in this study was constant in time. However,
550 the absorption efficiency of mineral dust can vary for each deposition event depending on the region of origin or the size distribution (*e.g.*, Dumont et al. (2023); Caponi et al. (2017)), as well as by its location within the snowpack either inside or outside the snow grains (He et al., 2018) and by the aggregation state of the dust particles (Bond, Bergstrom, 2006). As shown in Fig. 8, a low and a high value of dust MAE (Section 2.4.1) strongly affects the resulting dust impact ($\Delta_{\text{dust}} < 0.4$ m w.e. for the low MAE and $\Delta_{\text{dust}} > 1.4$ m w.e. for a high MAE). However, these extreme dust impacts are unlikely since the simulations

555 using extreme dust MAE (low and high) results in degraded accuracy metrics with respect to in situ measurements compared to the reference scenario used throughout the study (not shown).

Finally, the maximum dust impact Δ_{dust} in our study was found in 2022. Given the extreme dust deposition event of February 2021 (Dumont et al., 2023), it might be surprising that the impact of dust in 2021 was lower than that of 2022. This shows that the impact of dust on the annual glacier SMB is not solely guided by the mass of dust deposited during the current year. 560 Indeed, in 2021, a total of 15.1 g m^{-2} of dust was deposited, whereas 13.1 g m^{-2} was deposited during year 2022, and the simulated dust impact Δ_{dust} at the glacier scale was 0.45 m w.e. in 2021, and 0.63 m w.e. in 2022. The impact of dust on the annual SMB results from a combination of factors including the meteorological conditions, the timing of dust deposition and the time duration of exposure at the snow surface. For the extreme melt of 2022, the abnormally hot temperatures since May 2022, and numerous heatwaves during the summer 2022 probably strengthened the impact of dust by inducing an early and 565 long exposure of dust on a part of the glacier. Moreover, the melt rate is also modulated by the reappearance of firn layers from previous years, *e.g.*, the highly contaminated firn of 2021 during the 2022 melt season. To conclude, in the same way than the long-term evolution of a glacier depends on its evolution during the past decades, the impact of mineral dust is not limited to its recent history of deposition: mineral dust could act as a positive feedback for several years after deposition, particularly in the accumulation area.

570 4.2 Uncertainties linked to black carbon

The reference BC scavenging efficiency k_{BC} used by previous studies is 0.2 (*e.g.*, Flanner et al., 2007; Gabbi et al., 2015), and we also chose this value in our reference simulation. Here, results showed that the sensitivity of the annual glacier SMB and dust impact to k_{BC} around 0.2 ($\pm 20 \%$) were two times lower than the sensitivity to BC deposition fluxes ($\pm 20 \%$) for year 2022 (Fig. 7). In other words, the intensity of BC deposition fluxes had here more influence on the annual glacier SMB 575 and dust impact than the scavenging efficiencies. For the SMB sensitivity, this result was different than in Gabbi et al. (2015) who found an absolute sensitivity to BC scavenging efficiency three times larger than to BC deposition fluxes. We noted that different time steps may explain such a difference depending on the numerical scheme (15 minutes in our study, 1 day in Gabbi et al., 2015).

Furthermore, multiple studies reported that k_{BC} is subject to large uncertainties: $k_{\text{BC}} \in [0.003, 2.0]$ depending on the BC 580 species in Flanner et al. (2007), $k_{\text{BC}} \in [0.02, 2.0]$ in Bond et al. (2013), $k_{\text{BC}} \in [0.02, 2.0]$ in Qian et al. (2014). Thus, we conducted a more detailed sensitivity study at the glacier scale by increasing k_{BC} from 0.2 to 1.0. Figure 8 illustrates that the associated annual glacier SMBs were still within the spread of the ensemble, with an increase in annual glacier SMB of 0.15-0.3 m w.e. that was small compared to a SMB of less than 3 m w.e. We also noted that this increase in glacier SMB was not linear with regard to k_{BC} , as demonstrated by Dumont et al. (2020) for the relationship between the shortening of the 585 snow melt period and the deposited mass of mineral dust. More importantly, the dust impact was significantly modified without modifying the dust deposition fluxes: increasing k_{BC} from 0.2 to 1.0 doubled the dust impact from 0.63 to 1.3 m w.e. and the resulting dust impacts were not in the ensemble spread anymore. The reason behind this comes from the dependency of albedo on dust and BC, as shown in Equations (3) and (7) in Tuzet et al. (2020): the derivative of snow albedo with regard to dust

concentration, that is negative, is an increasing function of BC concentration. Hence, higher BC scavenging efficiencies lead to less BC at the snow surface, and to higher dust impacts.

Overall, the uncertainties on LAP scavenging efficiencies in snow result in large uncertainties on the respective absolute impacts of dust and BC. This highlights the need to better understand the motion of the different LAPs inside of the snowpack at the micro-scale. Here, BC scavenging in snow, that is still not quantified properly in the European Alps, represents a significant source of uncertainty on the dust impact. However, our simulations estimated the respective impact of each impurity for varying scavenging efficiencies, showing that an increase in the simulated BC scavenging efficiency led to a higher simulated impact of dust.

4.3 Other limitations

Although we believe that our study contributes to a better understanding of the role of LAPs on the glacier SMB, our simulations were subject to multiple other limitations that are discussed below.

The values of ice albedo and roughness length were taken constant in time and space, while numerous studies showed that those parameters could vary significantly in time and across a glacier (*e.g.*, Brock et al., 2006; Oerlemans et al., 2009; Naegeli, Huss, 2017). However, the sensitivity study of Section 3.3 shows that although changing ice albedo values can moderately modify the glacier SMB, this only slightly modifies the dust impact at the glacier scale compared to other sensitivity tests, *e.g.*, mineral dust and BC deposition fluxes. Given that the uncertainty in ice albedo was estimated to be around 20 % of its reference value (Section 2.2.5), the assumption of taking a constant ice albedo does not impact the conclusions of the present study. For the roughness length, its value can vary by an order of magnitude, but the sensitivity of glacier dust impact to roughness length is negligible, so taking a constant roughness length value does not modify the conclusion of this study.

The evaluation of the simulated SMB against point measurements and S2 images shows that the spread of simulated SMB was large and covers a wide range of scenarios, although this appears necessary to cover uncertainties at each measurement point. In the accumulation area, the RMSE of the summer melt against point measurements are of the same order of magnitude than that at lower elevation, but the summer melt is lower, resulting in larger relative uncertainties. However, the point measurements in the accumulation area are subject to larger uncertainties due to: (i) preferential accumulation, or (ii) human errors in distinguishing seasonal snow from old firn and measuring large snow accumulations. For instance, the measurement location associated with point P3 is known to be located in an area with preferential snow accumulation (which results in an observed SMB often higher than the simulated SMB in Fig. 5c). Such a measurement may then not be representative of the 250 by 250 m surrounding area.

The spatially distributed evaluation of the simulation against the Pléiades-derived SMB showed that the spread of the simulated SMB was not sufficient to capture the highest snow accumulation at the base of the north-east facing headwalls. This low accumulation at the base of the headwalls translated into a lower simulated SMB at the glacier scale, *e.g.*, $-1.9 \text{ m w.e yr}^{-1}$ simulated vs. $-0.59 \text{ m w.e yr}^{-1}$ for the Pléiades SMB over the period 2018-2022. Steep surrounding slopes are known to be prone to frequent avalanches from the headwalls onto the Argentière Glacier as demonstrated by Kneib et al. (2024a). To account for avalanches, one could argue that we could have artificially amplified precipitations, *e.g.*, using a simple avalanche model like

Snowslide (Bernhardt, Schulz, 2010), which may lead to better evaluation results. But at the same time, it is highly unclear how LAPs redistribute within the snow during such events. Are they redistributed? If so, do they redistribute homogeneously, at the top or under the transported snow? Because of a lack of knowledge regarding those issues, we did not model this process. To sum up, our simulation lacked snow accumulation at the base of the headwalls, presumably due to avalanches, therefore the results at these particular locations need to be taken with caution, and this could slightly modulate the dust impact at the glacier scale.

Other LAPs than mineral dust and BC in snow might also impact glacier albedo. Red snow algae are known to lower snow albedo in spring and summer in the European Alps (*e.g.*, Ezzedine et al., 2023). However, Roussel et al. (2024) have shown that their presence over Argentière Glacier was very limited. Indeed, the total area with at least one retrieval of red algal blooms over the period 2018-2022 represents less than 1 % of the area of the Argentière Glacier. Based on this, we did not consider snow algae in this study, because their impact would have been small compared to other LAPs. Brown carbon is also known to increase light absorption in the snowpack. Its optical properties, atmospheric concentrations and deposition fluxes are still under large uncertainties, however we believe that the impact of brown carbon is lower than that of BC (Skiles et al., 2018). In addition, mineral dust from local sources, *e.g.*, surrounding moraines, might also contribute to lower the glacier albedo (*e.g.*, Oerlemans et al., 2009). On annual snow, however, we assumed that their impact was relatively small compared to dust and BC.

The uncertainties in the results can also be related to the choice of the model and the parameters used in the model (*e.g.*, Lafaysse et al. (2017)). In this study, this primarily concerns the physical processes driving snow evolution and the radiative transfer model. Concerning the radiative transfer model, here TARTES coupled with the snow model, comparisons between radiative models (SNICAR and TARTES in G. Picard, Q. Libois (2024)) indicate that the choice of the radiative transfer model has a significantly smaller impact on the results than variations in the optical properties of the LAP, here represented using the MAE of each LAP. Therefore, the uncertainty related to the radiative model is fully accounted for in this study by varying the dust MAE factor (Section 4.1). Concerning the snow model, an ensemble approach can provide estimates of snow model uncertainties. Réveillet et al. (2022) applied this method to Crocus and reported results on the impact of the LAPs comparable to deterministic simulations (Supplementary Fig. S10 of Réveillet et al. (2022)). Furthermore, uncertainties related to the snow model choice are generally smaller than those associated with the forcing (*e.g.*, Etchevers et al. (2004); Günther et al. (2019)). To explore the uncertainties related to the meteorological variables, we did the choice to use an ensemble of forcing produced using stochastic perturbations on the adjusted SAFRAN data (Section 2.3.6). Ultimately, the dust impact presented in this study is expressed as relative differences between simulations rather than as absolute values, which limits the influence of uncertainties related to the forcing and to the snow model choice.

Finally, the deposition of LAPs was constant in space in this study. As underlined by Warren (2019), there is still a lack of knowledge about the heterogeneity of LAPs deposition at the small scale depending on topographic characteristics. For example, in the European Alps during the extreme dust event of February 2021, Dumont et al. (2023) showed that south-facing slopes had received higher dust quantities by up to one order of magnitude compared to other orientations, probably due to the trajectory of the dust transport coming from the South during this event. These preferential depositions were not taken into

account in our simulations and further research will be needed to understand their impacts. Nevertheless, we may expect a higher impact of dust on south-facing slopes because of: (i) higher dust deposition; and (ii) higher shortwave radiation. Finally, one may also wonder whether the deposited quantities of LAPs are the same at all elevations.

Besides those modelling limitations, an extension of this method to other glaciers would also rely on the availability of computational cost and resource usage. In this study, the simulations with the snowpack model SURFEX/ISBA-Crocus, including 2x40 members (with and without dust) and around 40 sensitivity tests over the period 2008-2022 with 179 distributed points, lasted 0.75 h parallelized on 15,360 CPU (total of 480 days of CPU time), needed around 100 MJ, *i.e.*, around 25 kWh, and emitted approximately 6 kg of CO₂ equivalent.

5 Conclusions

Here, we simulated the SMB of the Argentière Glacier during the years 2019-2022, ending with the exceptional melt of 2022 in the European Alps. We used the SAFRAN meteorological reanalysis adjusted with local observations and the LAP deposition fluxes from ALADIN as inputs for the SURFEX/ISBA-Crocus snow model at 250 m horizontal resolution. The resulting SMBs were evaluated using various data: summer point SMB measurements, Sentinel-2 images and Pléiades-derived distributed SMB. Embedded in the snow model, a radiative transfer model enabled quantifying accurately the impact of mineral dust inside snow.

For years 2019-2021, the lowering of the glacier-wide annual SMB due to mineral dust was between 0.31-0.45 m w.e. [0.30, 0.49], representing 9.1-14.7 % [8.3, 16.1] of the total annual melt. However, during the exceptional melt of 2022 the impact of dust increased to 0.63 m w.e. [0.54, 0.69] representing 13.2 % [11.8, 14.7] of the total melt. This year, depending on the location on the Argentière Glacier, LAPs had very different impacts on the SMB: between 0-0.5 m w.e. in the ablation area where ice was exposed during most of the melt season, between 0.4-0.8 m w.e. at higher elevation in the accumulation area where the glacier was permanently covered with snow, and the highest impacts, between 0.4-1.2 m w.e. were found in the vicinity of the end-of-summer snowline. At that latter location, the impact of mineral dust in 2022 rose up to 1.20 m w.e., representing more than 20 % of the total annual melt. We also showed that the impact of LAPs over the glacier was not simply correlated with recent depositions: due to melt, stacked LAPs in old buried firn layers from previous years could reappear at the snow surface, hence also contributing to lowering the albedo. This also means that the impact of LAPs is strongly modulated by meteorological conditions. Thus, taking LAPs into account in glacier melt requires a long-term memory both for the meteorological conditions and LAP deposition fluxes.

Our approach encountered some limitations at specific locations, such as at the base of the steep glacier headwalls where snow redistribution by avalanches strongly increases snow accumulation. Simulating this process would likely modify the simulated impact of dust at these locations. Furthermore, large uncertainties linked to the percolation of BC within the snowpack might lead to significantly higher impacts of dust. Using different mass absorption efficiency for the dust particles in snow also significantly modulated the results. Further research is needed to understand these processes and to quantify their impacts.

690 Since mineral dust in snow already accounts for around 8-16 % of the total annual melt for the Argentière Glacier for the
period 2019-2022, its impact can not be totally neglected in past simulations and for future projections. Moreover, if we had
considered mineral dust in ice, the impact on the surface mass balance could be higher. While quantifying the impact of LAPs
locally and at a given date can be achieved using observation, modelling is required to estimate the past and future impact
of LAPs over large spatial and temporal scales. The simulation setup of this study is easily transferable in time and space
695 for glaciers where measurements of winter solid precipitation and summer melt exist. An automatic weather station is also
useful to ensure the accuracy of the meteorological forcings used in the model. As a result, this work paves the way towards a
comprehensive regional assessment of the impacts of LAPs on glaciers in monitored regions.

Code availability. We used the open-source SURFEX project in this study. The procedure to access the code is described at <https://github.com/UMR-CNRM/snowtools/blob/master/doc/source/misc/surfex-install.rst> (last access: 17 September 2025). The version used in this work
700 is tagged as *argentiere_glacier_roussel* in the git branch named *cen_dev_glacier*. More general information about SURFEX use can be found
at <https://github.com/UMR-CNRM/snowtools> (last access: 17 September 2025).

Data availability. Sentinel-2 products are distributed by Theia at <https://geodes-portal.cnes.fr>. SMB point measurements are distributed by
GLACIOCLIM at <https://glacioclim.osug.fr/>. SAFRAN meteorological forcings are distributed at <http://dx.doi.org/10.25326/37#v2024.1>.
Forcing files used in this study are available at <https://doi.org/10.5281/zenodo.17140557>.

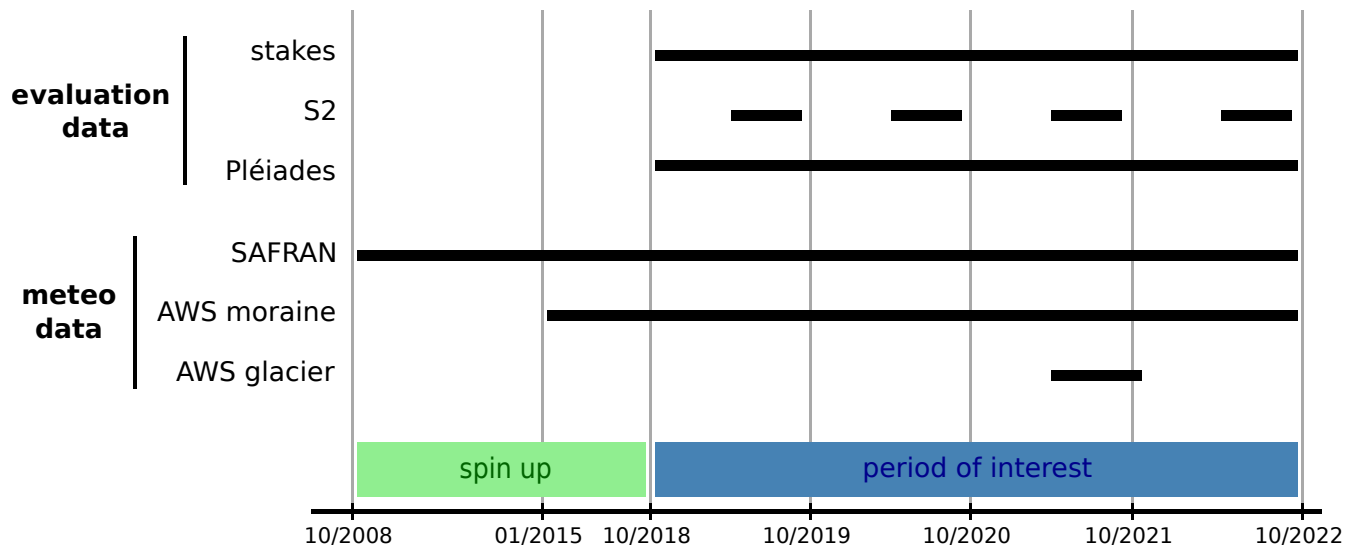


Figure A1. Availability and usage of each data sources. Black lines show data usage.

705 **Appendix A: Data Appendix**

Table B1. Dates of the selected Sentinel-2 images.

2019	2020	2021	2022
24/06	29/05	13/06	18/06
04/07	23/06	18/07	08/07
19/07	18/07	12/08	02/08
03/08	07/08	27/08	12/08
23/08	16/09	11/09	01/09
17/09			

Appendix B: Sentinel-2 Appendix

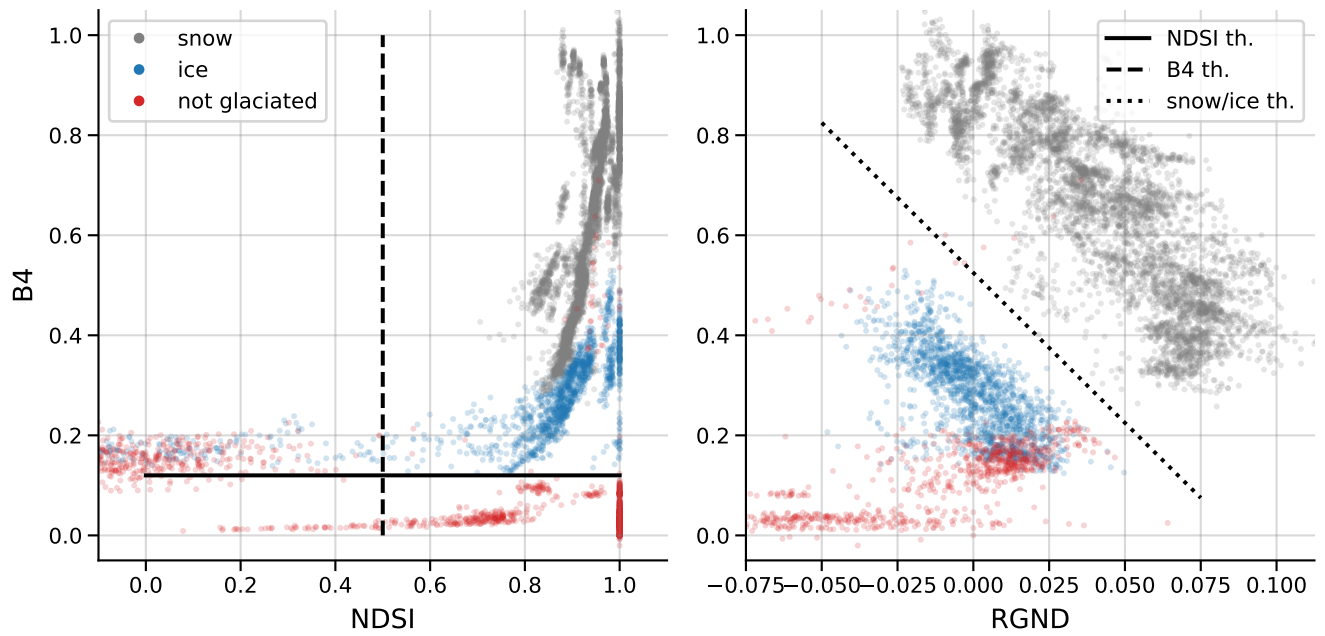


Figure B1. Distribution of the S2 labelled pixels over Argentière Glacier depending on reflectance R_{B4} , and indexes NDSI and RGND. The thresholds mentioned in Section 2.2.3 are represented by the 3 black lines. See Section 2.2.3 for more details.

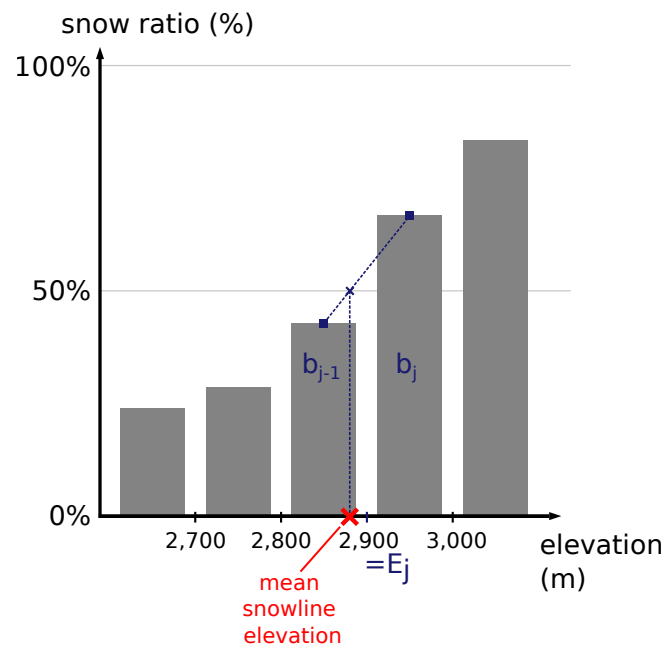


Figure B2. Illustration of the computation of the mean snowline elevation explained in Section 2.2.4.

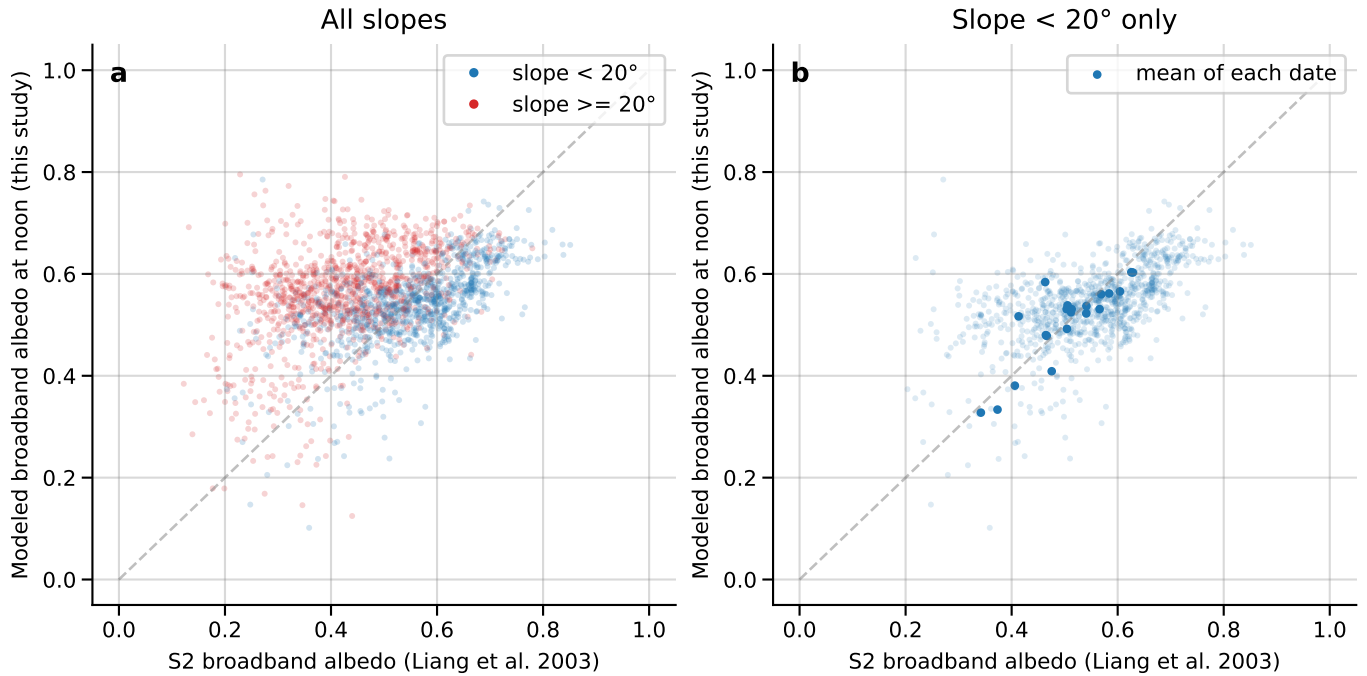


Figure B3. Comparison between simulated broadband albedo and broadband albedo derived from S2. See section 2.2.6 for methods and limitations. (a) Influence of the slope. (b) Comparison for slopes $< 20^\circ$. The mean of all dates, except 2, shows less than 0.1 of difference between the modelled albedo and the albedo derived from S2. This comparison of broadband albedo has to be taken with cautious. Indeed, there are several limitations. First, the broadband albedo derived from S2 (Liang et al., 2003) was not developed for snow, an anisotropic surface (e.g., Dumont et al. (2010)), i.e., the reflectance depends on the observation angle. Second, the uncertainties of the reflectance retrievals in complex terrain may be too high to estimate the accuracy of the simulated albedo, e.g., Cluzet et al. (2020), or panel (a) of this figure where the broadband albedo derived from S2 strongly depends on the slope.

Table C1. Sensors and the associated measurement accuracies for glacier and moraine AWSs.

	Temperature	Q	Wind	SW	LW
glacier AWS	HMP155A	HMP155A	Young05103	NR01	NR01
uncertainty	$\pm(0.226 - 0.0028 \cdot T) \text{ }^\circ\text{C}$	$\pm(1.0 + 0.008 \cdot \text{reading}) \text{ \% RH}$	$\pm 0.3 \text{ m s}^{-1}$	10% of daily sum	10% of daily sum
moraine AWS	HMP155A	HMP155A	Young05103	CNR4	CNR4
uncertainty	$\pm(0.226 - 0.0028 \cdot T) \text{ }^\circ\text{C}$	$\pm(1.0 + 0.008 \cdot \text{reading}) \text{ \% RH}$	$\pm 0.3 \text{ m s}^{-1}$	10% of daily sum	10% of daily sum

Appendix C: Meteorological Appendix

Table C2. Comparison between seasonal mean of SAFRAN variables at the location of the moraine AWS (1) and observed variables from the moraine AWS (2). For variables T (air temperature, K), W (wind speed, m s^{-1}), LW (incoming longwave, W m^{-2}), SW (incoming shortwave, W m^{-2}) during winter/summer periods (1st October, 1st May).

Period	T ₁ (K)	T ₂ (K)	W ₁ (m s^{-1})	W ₂ (m s^{-1})	LW ₁ (W m^{-2})	LW ₂ (W m^{-2})	SW ₁ (W m^{-2})	SW ₂ (W m^{-2})
sum. 15	280.6	279.6	2.97	3.00	296.9	294.4	234.9	222.4
win. 15-16	271.3	270.7	3.83	3.46	241.8	256.7	109.4	110.8
sum. 16	279.9	278.9	2.73	2.66	297.5	289.4	223.5	225.1
win. 16-17	271.2	270.7	3.51	3.23	232.5	263.5	121.1	114.1
sum. 17	280.1	279.6	2.83	2.96	299.4	314.1	212.9	209.1
win. 17-18	269.9	270.1	3.53	3.50	242.7	272.9	109.8	113.3
sum. 18	280.7	280.5	1.86	2.43	306.2	319.0	225.7	219.8
win. 18-19	270.7	270.8	3.50	3.37	244.4	246.6	116.5	120.0
sum. 19	280.4	280.1	2.48	2.90	298.5	293.6	248.7	232.8
win. 19-20	271.9	271.8	3.44	3.82	249.8	254.3	116.2	112.8
sum. 20	280.1	279.9	2.23	2.71	303.7	296.2	236.7	229.0
win. 20-21	270.1	269.9	3.11	3.14	243.9	250.0	115.4	119.1
sum. 21	280.6	280.1	2.96	2.93	298.7	294.5	234.2	218.4
win. 21-22	271.6	271.1	3.46	2.96	235.2	240.9	126.8	125.6
sum. 22	281.9	281.2	2.73	2.99	306.8	296.5	248.7	237.5

C1 Stochastic perturbations of the meteorological forcings

The method is inspired from Charrois et al. (2016). Air temperature and longwave radiation are perturbed as additive variables, and shortwave radiation, wind and precipitations are perturbed as multiplicative variables. σ_X is estimated for each variable using the standard deviation of the difference between the modelled and the observed variable.

Given an additive variable V_t at time-step t , the perturbed variable V_t^* is defined as

$$V_t^* = V_t + X_t \quad (C1)$$

and in case the variable is multiplicative, V_t^* is defined as

$$V_t^* = V_t \cdot (1 + X_t) = V_t + V_t \cdot X_t \quad (C2)$$

In both cases, the perturbed term X_t is built using an autoregressive model of order one (AR(1))

$$X_t = \phi \cdot X_{t-1} + \epsilon_t(\sigma_\epsilon) \quad (C3)$$

with $\phi = \exp(-dt/\tau)$, the time-step dt , the decorrelation time τ (such as $\tau > dt$, and X_t is weak-sense stationary), and a white noise ϵ_t of variance σ_ϵ^2 . The parameter σ_ϵ could be retrieved for each variable.

For additive variables, by applying the variance to the perturbed term X of Equation C1, we find

$$\sigma_\epsilon = \sqrt{(1 - \phi^2)} \cdot \sigma_X \quad (C4)$$

where σ_X is the standard deviation of X . In this case, σ_ϵ has the same dimension as X .

For multiplicative variables, by applying the variance to the perturbed term $V \cdot X$ of Equation C2, with X and V independents, and σ and μ the standard deviation and mean of a variable, we have

$$\sigma_{V \cdot X}^2 = \sigma_V^2 \cdot \sigma_X^2 + \sigma_V^2 \cdot \mu_X^2 + \sigma_X^2 \cdot \mu_V^2 \quad (C5)$$

with $\mu_X = 0$ and $\sigma_\epsilon^2 = (1 - \phi^2) \cdot \sigma_X^2$, we find

$$\sigma_\epsilon = \sqrt{1 - \phi^2} \cdot \frac{\sigma_X}{\sqrt{\sigma_V^2 + \mu_V^2}} \quad (C6)$$

In this case, σ_ϵ has no dimension.

In practice, for multiplicative variables, if the term $(1 + X_t)$ was lower than 0, the value of $(1 + X_t)$ was set to 0 to avoid setting negative values for meteorological variables such as wind or shortwave radiation. However, when the ratio $\frac{\sigma_X}{\sqrt{\sigma_V^2 + \mu_V^2}}$ was higher than 0.42, $(1 + X_t)$ was set to 0 with a probability of around 1%. This was artificially increasing the mean of the perturbed variable. Hence, to avoid this behavior, we bounded the values of $(1 + X_t)$ between 0 and 2 (as in Charrois et al. (2016) that bounded $(1 + X_t)$ between 0.5 and 1.5).

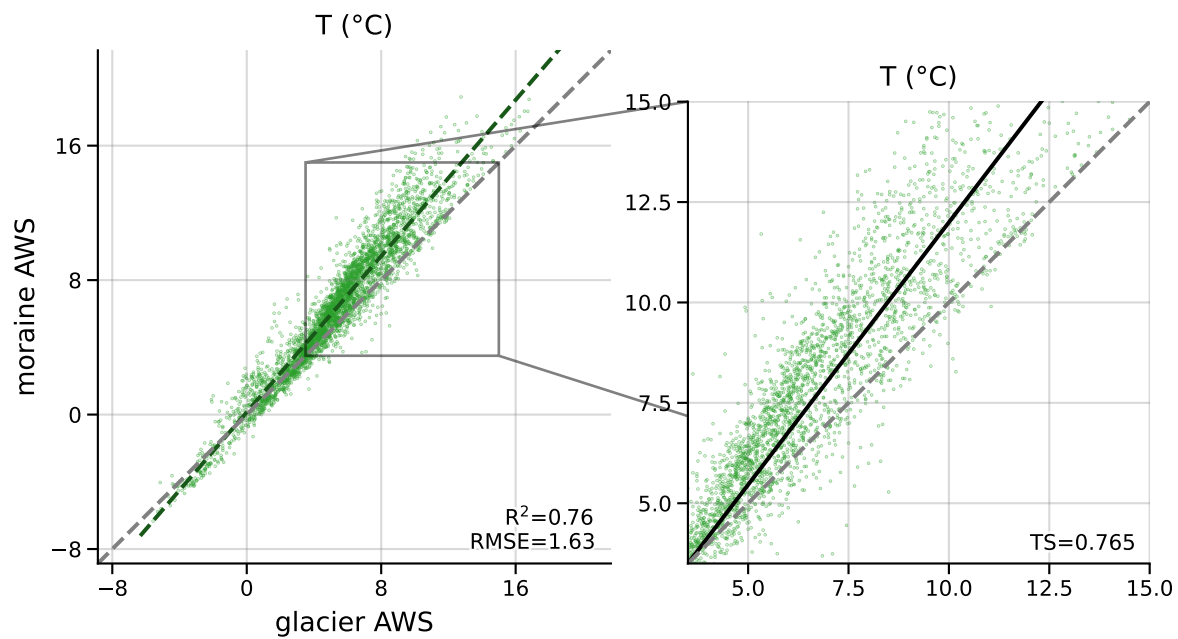


Figure C1. Comparison of the air temperatures between glacier and moraine AWS from 05/20/2021 to 22/10/2021. Grey dotted line represents 1:1 line. Colored dotted line represents the associated linear regression at all time-step. Zoomed plot shows air temperatures only above 3.5 °C. The solid green line is the linear regression with a zero intercept at 3.5 °C only for temperatures above 3.5 °C. TS is the the resulting temperature sensitivity.

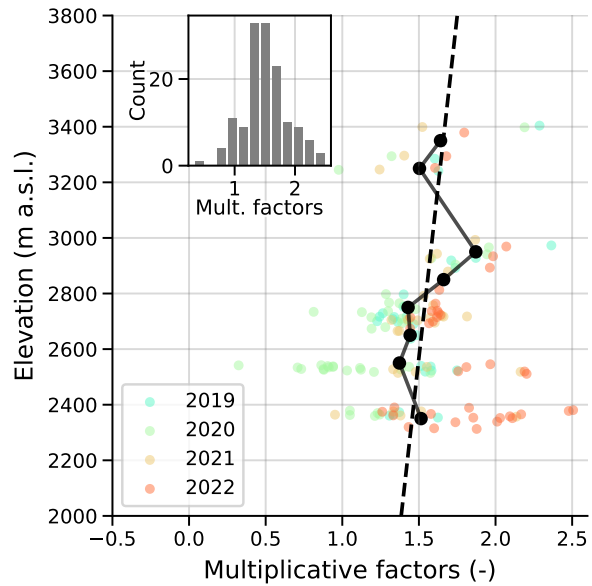


Figure C2. (a) Solid precipitation multiplicative factors, for each point accumulation measurements and four winter accumulations (colored dots), aggregated over 100 m bin (black dots), and linearly interpolated (dashed black line). Year N refers to winter accumulation between autumn N-1 to spring N. (b) Histogram of the multiplicative factors for each winter point accumulation measurements from 2019 to 2022 (colored dots from panel (a)).

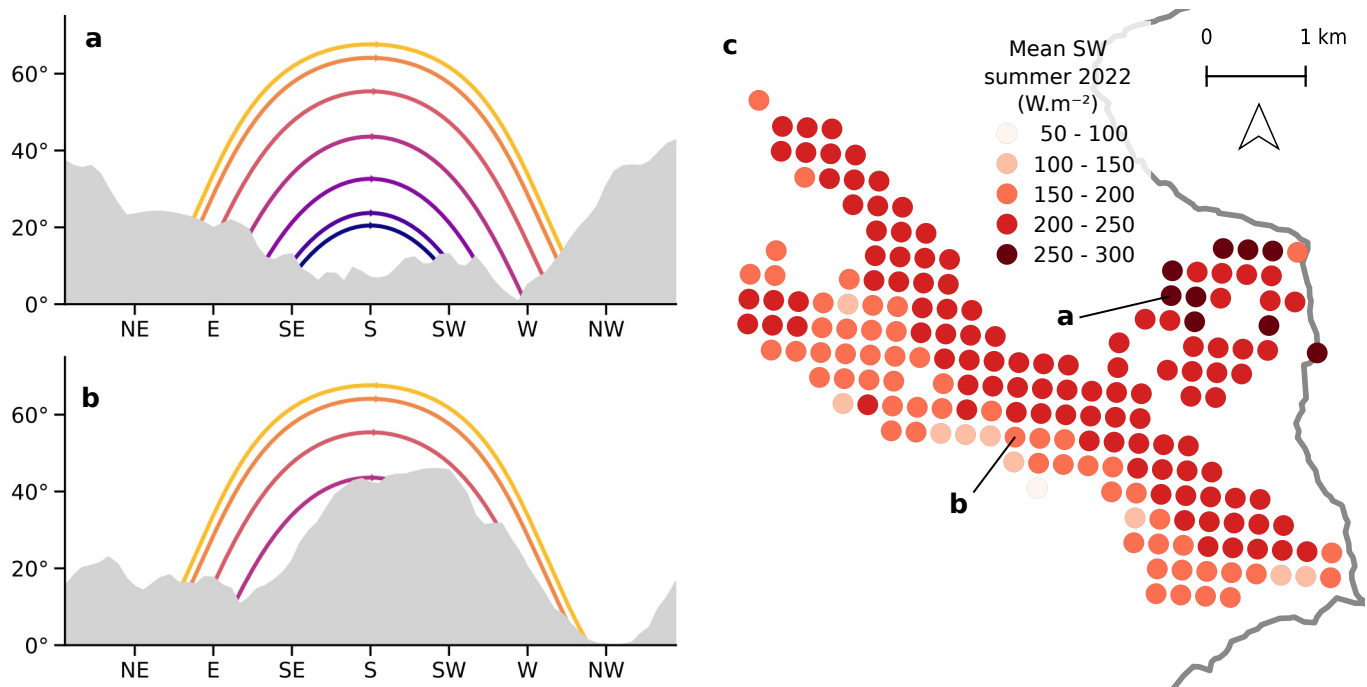


Figure C3. (a, b) Example of illumination masks at two locations over Argentière Glacier. Aspect resolution is 5°. The lines represent the sun trajectories (from top to bottom) on 21th Jun. (yellow line), 21th May and 21th Jul., 21th Apr. and 21th Aug., 21th Mar. and 21th Sept., 21th Feb. and 21th Oct., 21th Jan and 21th Nov., 21th Dec. (blue line). (c) Mean shortwave radiation during summer 2022 (01/05 to 30/09) from SAFRAN with illumination masks.

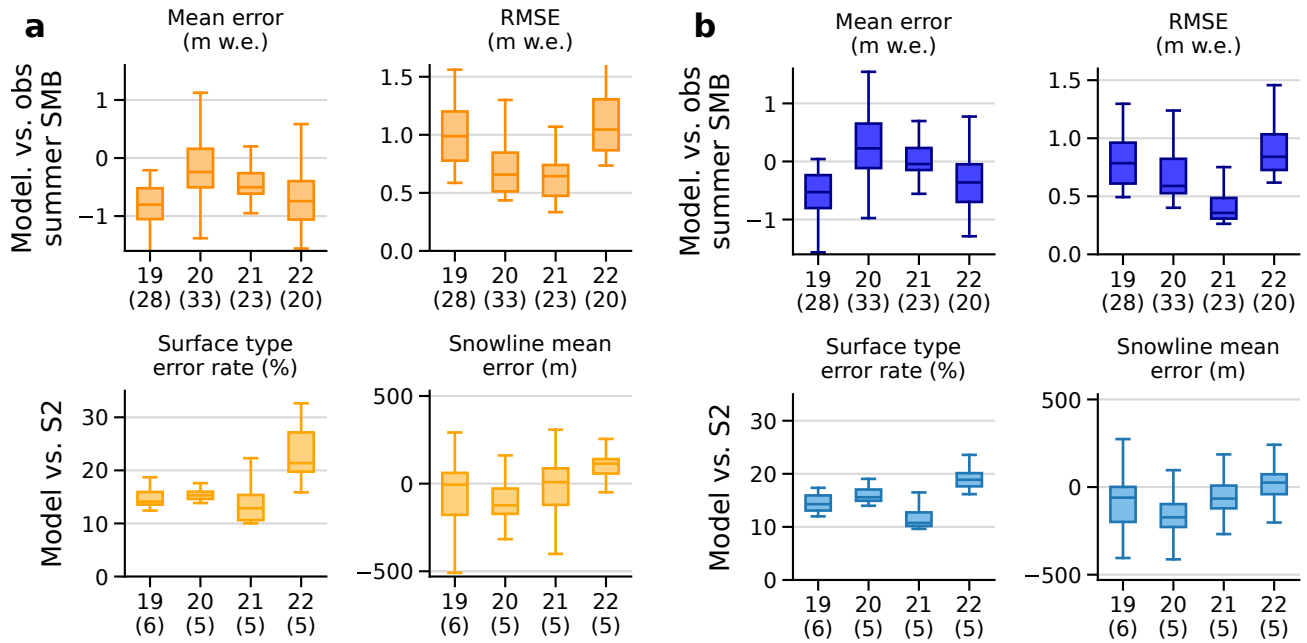


Figure D1. Extension of Fig. 3 with (a) dust simulations in orange (analogous to Fig 3), and (b) no-dust simulations in blue.

Appendix D: Evaluation extension

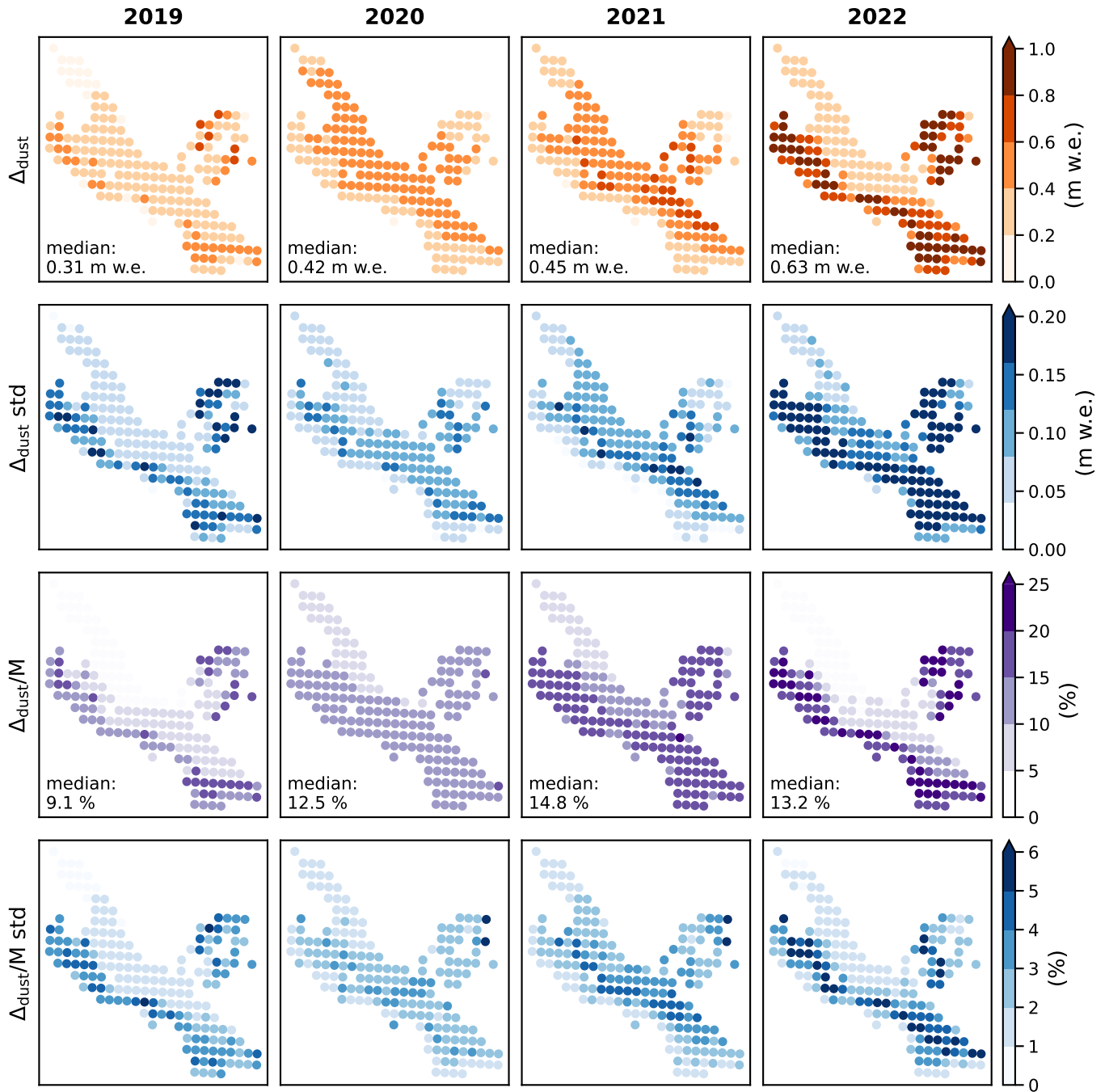


Figure E1. Extension of Fig. 6 for the years 2019 to 2022. Dust impact Δ_{dust} and melt fraction Δ_{dust}/M with the associated standard deviation of the ensemble. The median of the ensemble is represented at each point. The aggregated value refers to the median (over the 40 members) of the mean over all simulation points.

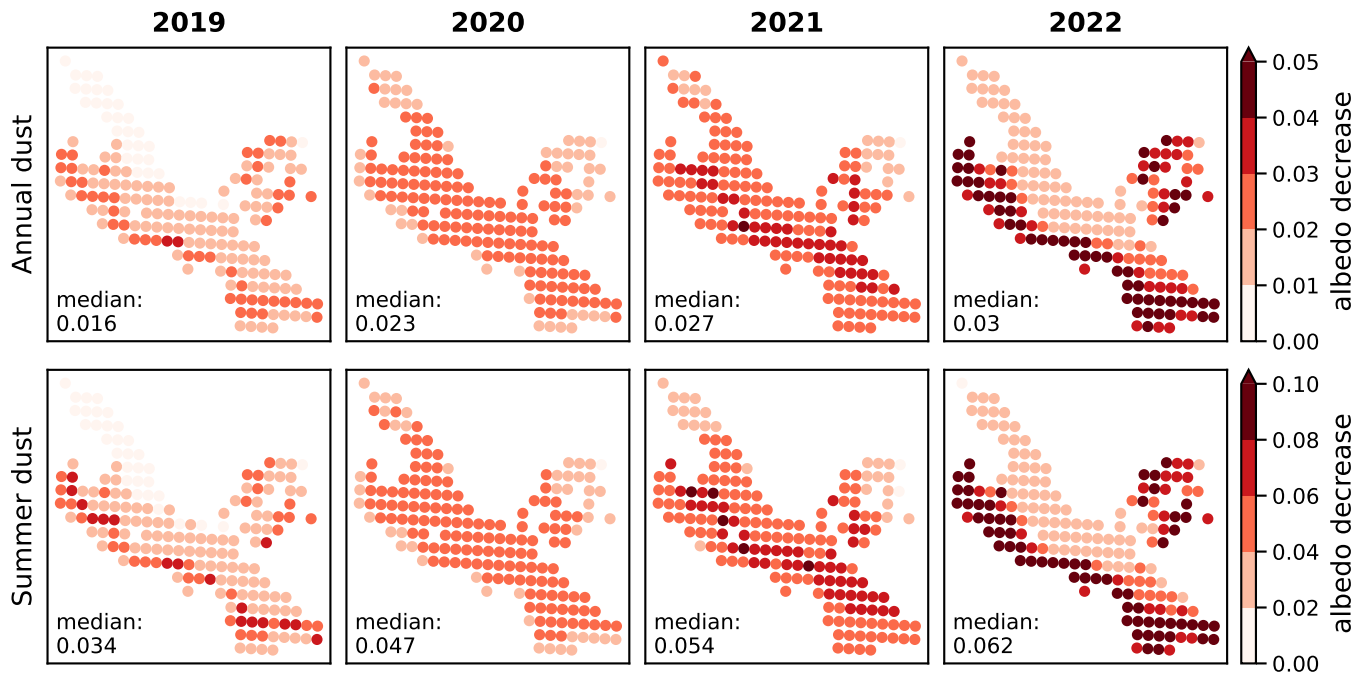


Figure E2. Extension of Fig. 6 for the years 2019 to 2022. Annual and summer albedo decrease due to dust. The median of the ensemble is represented at each point. The aggregated value refers to the median (over the 40 members) of the mean over all simulation points.

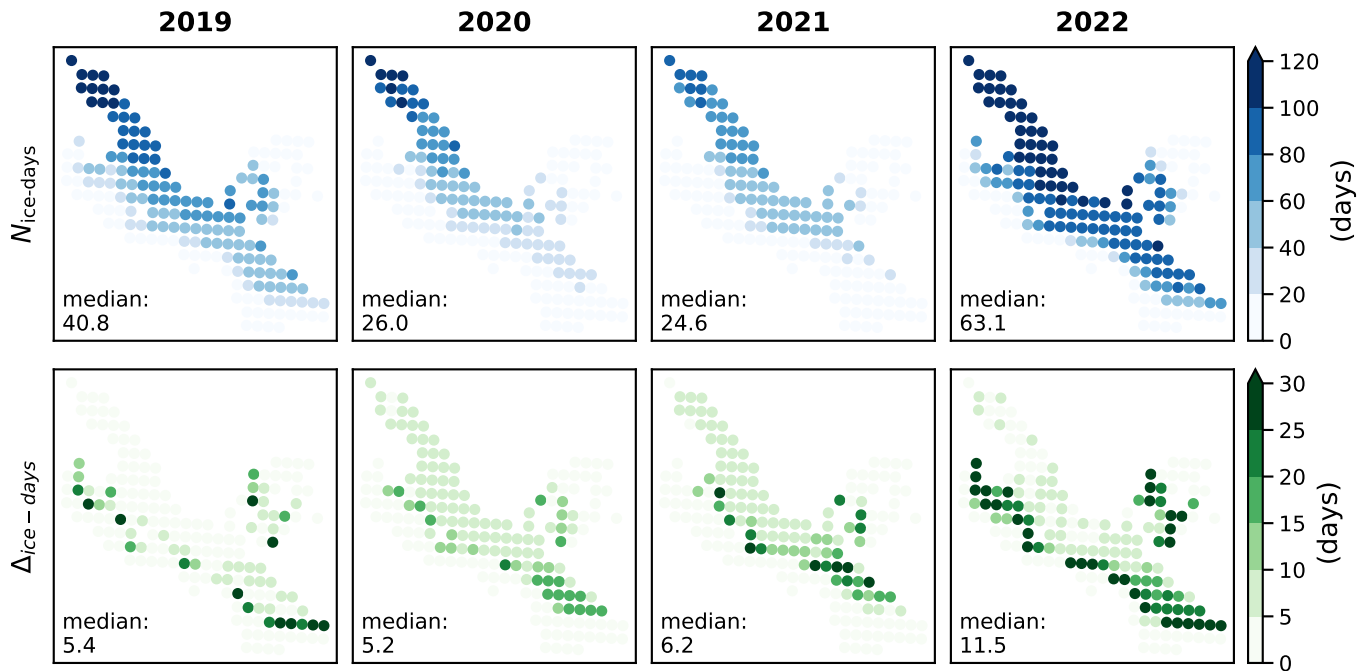


Figure E3. Extension of Fig. 6 for the years 2019 to 2022. Number of days with ice exposed at the surface for the dust simulation, and number of days with ice exposed for the dust simulation but not for the no-dust simulations. The median of the ensemble is represented at each point. The aggregated value refers to the median (over the 40 members) of the mean over all simulation points.

Author contributions. LR led the study, performed the simulation and analysis. MD, MR and DS designed the study and supervised the writing the manuscript. MK provided the Pléiades SMB and supported their analysis. PN provided the ALADIN deposition fluxes. KF and DM advised for the model development and data analysis. SG provided the S2 data and helped for their analysis. ET, MB, LP, OL and BJ provided the in-situ mass balance data and the automatic weather station data, and helped with the data analysis. MF, MV and ML advised for the model development and supervised the HPC computation. AR and JMS contributed to the data analysis. LR wrote the article with contribution of all co-authors.

Competing interests. Some authors are members of the editorial board of journal The Cryosphere.

Acknowledgements. CNRM/CEN and IGE are part of Labex OSUG@2020 (ANR-10-LABX-0056). Léon Roussel, Marie Dumont and Kévin Fourteau have received funding from the European Research Council (ERC) under the European Union's Horizon 2020 research and innovation programme (grant agreement no. 949516, IVORI). Marin Kneib acknowledges the funding from the Swiss National Science Foundation (SNSF) under the Postdoc Mobility program (grant agreement P500PN-210739, CAIRN). We thank the GLACIOCLIM monitoring service (CNRS-INSU, UGA-OSUG, IRD, INRAE, IPEV, Météo France) for the in situ surface mass balance measurements (<https://glacioclim.osug.fr/>, last access: 28/03/2025), and all those who conducted these field measurements. We also thank the ANR SAUS-SURE for the AWS measurements (ANR-18-CE01-0015-01 Sliding of glAciers and sUbglaical water pressure). We are grateful to the DINAMIS initiative (<https://dynamis.data-terra.org/>, last access: 28/03/2025) that supports the access to Pléiades data for the French academic sector. The authors thank Mathias Huss, Bertrand Cluzet, Giulia Mazzotti and Ghislain Picard for fruitful discussions.

References

- Arnold Neil S., Rees W. Gareth, Hodson Andrew J., Kohler Jack. Topographic controls on the surface energy balance of a high Arctic valley glacier // *Journal of Geophysical Research: Earth Surface*. 2006. 111, F2. _eprint: <https://onlinelibrary.wiley.com/doi/pdf/10.1029/2005JF000426>.
755
- Baba Mohamed Wassim, Gascoïn Simon, Kinnard Christophe, Marchane Ahmed, Hanich Lahoucine. Effect of Digital Elevation Model Resolution on the Simulation of the Snow Cover Evolution in the High Atlas // *Water Resources Research*. 2019. 55, 7. 5360–5378. _eprint: <https://onlinelibrary.wiley.com/doi/pdf/10.1029/2018WR023789>.
- Baladima Foteini. Modeling the impact of air pollution deposition on the alpine snow lifecycle. XII 2021.
- Bernhardt M., Schulz K. SnowSlide: A simple routine for calculating gravitational snow transport // *Geophysical Research Letters*. 2010. 37, 11. _eprint: <https://onlinelibrary.wiley.com/doi/pdf/10.1029/2010GL043086>.
760
- Berthier Etienne, Vincent Christian, Six Delphine. Exceptional thinning through the entire altitudinal range of Mont-Blanc glaciers during the 2021/22 mass balance year // *Journal of Glaciology*. 2023. 1–6. Publisher: Cambridge University Press.
- Bond T. C., Doherty S. J., Fahey D. W., Forster P. M., Berntsen T., DeAngelo B. J., Flanner M. G., Ghan S., Kärcher B., Koch D., Kinne S., Kondo Y., Quinn P. K., Sarofim M. C., Schultz M. G., Schulz M., Venkataraman C., Zhang H., Zhang S., Bellouin N., Guttikunda S. K., Hopke P. K., Jacobson M. Z., Kaiser J. W., Klimont Z., Lohmann U., Schwarz J. P., Shindell D., Storelvmo T., Warren S. G., Zender C. S. Bounding the role of black carbon in the climate system: A scientific assessment // *Journal of Geophysical Research: Atmospheres*. 2013. 118, 11. 5380–5552. _eprint: <https://onlinelibrary.wiley.com/doi/pdf/10.1002/jgrd.50171>.
765
- Bond Tami C., Bergstrom Robert W. Light Absorption by Carbonaceous Particles: An Investigative Review // *Aerosol Science and Technology*. I 2006. 40, 1. 27–67. Publisher: Taylor & Francis _eprint: <https://doi.org/10.1080/02786820500421521>.
770
- Brock Ben W., Willis Ian C., Sharp Martin J. Measurement and parameterization of aerodynamic roughness length variations at Haut Glacier d’Arolla, Switzerland // *Journal of Glaciology*. I 2006. 52, 177. 281–297.
- Caponi Lorenzo, Formenti Paola, Massabó Dario, Di Biagio Claudia, Cazaunau Mathieu, Pangui Edouard, Chevaillier Servanne, Landrot Gautier, Andreae Meinrat O., Kandler Konrad, Piketh Stuart, Saeed Thuraya, Seibert Dave, Williams Earle, Balkanski Yves, Prati Paolo, Doussin Jean-François. Spectral- and size-resolved mass absorption efficiency of mineral dust aerosols in the shortwave spectrum: a simulation chamber study // *Atmospheric Chemistry and Physics*. VI 2017. 17, 11. 7175–7191. Publisher: Copernicus GmbH.
775
- Charrois Luc, Cosme Emmanuel, Dumont Marie, Lafaysse Matthieu, Morin Samuel, Libois Quentin, Picard Ghislain. On the assimilation of optical reflectances and snow depth observations into a detailed snowpack model // *The Cryosphere*. V 2016. 10, 3. 1021–1038.
- Cluzet Bertrand, Revuelto Jesus, Lafaysse Matthieu, Tuzet François, Cosme Emmanuel, Picard Ghislain, Arnaud Laurent, Dumont Marie. Towards the assimilation of satellite reflectance into semi-distributed ensemble snowpack simulations // *Cold Regions Science and Technology*. II 2020. 170. 102918.
780
- Collaud Coen M., Weingartner E., Schaub D., Hueglin C., Corrigan C., Henning S., Schwikowski M., Baltensperger U. Saharan dust events at the Jungfraujoch: detection by wavelength dependence of the single scattering albedo and first climatology analysis // *Atmospheric Chemistry and Physics*. XII 2004. 4, 11/12. 2465–2480. Publisher: Copernicus GmbH.
- Conway H., Gades A., Raymond C. F. Albedo of dirty snow during conditions of melt // *Water Resources Research*. 1996. 32, 6. 1713–1718. _eprint: <https://onlinelibrary.wiley.com/doi/pdf/10.1029/96WR00712>.
785

- Cremona Aaron, Huss Matthias, Landmann Johannes Marian, Borner Joël, Farinotti Daniel. European heat waves 2022: contribution to extreme glacier melt in Switzerland inferred from automated ablation readings // *The Cryosphere*. V 2023. 17, 5. 1895–1912. Publisher: Copernicus GmbH.
- 790 Cuffey K.M., Paterson W.S.B. The physics of glaciers. // *Journal of Glaciology*. 2010. 57, 202. 383–384.
- Di Mauro B., Fava F., Ferrero L., Garzonio R., Baccolo G., Delmonte B., Colombo R. Mineral dust impact on snow radiative properties in the European Alps combining ground, UAV, and satellite observations // *Journal of Geophysical Research: Atmospheres*. 2015. 120, 12. 6080–6097. _eprint: <https://onlinelibrary.wiley.com/doi/pdf/10.1002/2015JD023287>.
- Di Mauro B., Garzonio R., Ravasio C., Orlandi V., Baccolo G., Gilardoni S., Remias D., Leoni B., Rossini M., Colombo R. Combined effect of algae and dust on snow spectral and broadband albedo // *Journal of Quantitative Spectroscopy and Radiative Transfer*. IV 2024. 316. 108906.
- Di Mauro Biagio, Garzonio Roberto, Rossini Micol, Filippa Gianluca, Pogliotti Paolo, Galvagno Marta, Cella Umberto Morra di, Migliavacca Mirco, Baccolo Giovanni, Clemenza Massimiliano, Delmonte Barbara, Maggi Valter, Dumont Marie, Tuzet François, Lafaysse Matthieu, Morin Samuel, Cremonese Edoardo, Colombo Roberto. Saharan dust events in the European Alps: role in snowmelt and geochemical characterization // *The Cryosphere*. IV 2019. 13, 4. 1147–1165. Publisher: Copernicus GmbH.
- 800 Doherty Sarah J., Grenfell Thomas C., Forsström Sanja, Hegg Dean L., Brandt Richard E., Warren Stephen G. Observed vertical redistribution of black carbon and other insoluble light-absorbing particles in melting snow // *Journal of Geophysical Research: Atmospheres*. 2013. 118, 11. 5553–5569. _eprint: <https://onlinelibrary.wiley.com/doi/pdf/10.1002/jgrd.50235>.
- Dozier Jeff. Spectral signature of alpine snow cover from the landsat thematic mapper // *Remote Sensing of Environment*. IV 1989. 28. 9–22.
- 805 Dumont M., Brissaud O., Picard G., Schmitt B., Gallet J.-C., Arnaud Y. High-accuracy measurements of snow Bidirectional Reflectance Distribution Function at visible and NIR wavelengths – comparison with modelling results // *Atmospheric Chemistry and Physics*. III 2010. 10, 5. 2507–2520. Publisher: Copernicus GmbH.
- Dumont M., Tuzet F., Gascoïn S., Picard G., Kutuzov S., Lafaysse M., Cluzet B., Nheili R., Painter T. H. Accelerated Snow Melt in the Russian Caucasus Mountains After the Saharan Dust Outbreak in March 2018 // *Journal of Geophysical Research: Earth Surface*. 2020. 125, 9. e2020JF005641. _eprint: <https://onlinelibrary.wiley.com/doi/pdf/10.1029/2020JF005641>.
- 810 Dumont Marie, Durand Yves, Arnaud Yves, Six Delphine. Variational assimilation of albedo in a snowpack model and reconstruction of the spatial mass-balance distribution of an alpine glacier // *Journal of Glaciology*. I 2012. 58, 207. 151–164. Publisher: Cambridge University Press.
- 815 Dumont Marie, Gascoïn Simon, Réveillet Marion, Voisin Didier, Tuzet François, Arnaud Laurent, Bonnefoy Mylène, Bacardit Peñarroya Montse, Carmagnola Carlo, Deguine Alexandre, Diacre Aurélie, Dürr Lukas, Evrard Olivier, Fontaine Firmin, Frankl Amaury, Fructus Mathieu, Gandois Laure, Gouttevin Isabelle, Gherab Abdelfateh, Hagenmuller Pascal, Hansson Sophia, Herbin Hervé, Josse Béatrice, Jourdain Bruno, Lefevre Irene, Le Roux Gaël, Libois Quentin, Liger Lucie, Morin Samuel, Petitprez Denis, Robledano Alvaro, Schneebeli Martin, Salze Pascal, Six Delphine, Thibert Emmanuel, Trachsel Jürg, Vernay Matthieu, Viallon-Galinier Léo, Voiron Céline. Spatial variability of Saharan dust deposition revealed through a citizen science campaign // *Earth System Science Data*. VII 2023. 15, 7. 3075–3094. Publisher: Copernicus GmbH.
- 820 Etchevers Pierre, Martin Eric, Brown Ross, Fierz Charles, Lejeune Yves, Bazile Eric, Boone Aaron, Dai Yong-Jiu, Essery Richard, Fernandez Alberto, Gusev Yeugeniy, Jordan Rachel, Koren Victor, Kowalczyk Eva, Nasonova N. Olga, Pyles R. David, Schlosser Adam, Shmakin

- 825 *Andrey B., Smirnova Tatiana G., Strasser Ulrich, Verseghy Diana, Yamazaki Takeshi, Yang Zong-Liang.* Validation of the energy budget of an alpine snowpack simulated by several snow models (Snow MIP project) // *Annals of Glaciology*. I 2004. 38. 150–158.
- Ezzedine Jade A., Uwizeye Clarisse, Si Larbi Grégory, Villain Gaelle, Louwagie Mathilde, Schilling Marion, Hagenmuller Pascal, Gallet Benoît, Stewart Adeline, Petroustos Dimitris, Devime Fabienne, Salze Pascal, Liger Lucie, Jouhet Juliette, Dumont Marie, Ravanel Stéphane, Amato Alberto, Valay Jean-Gabriel, Jounneau Pierre-Henri, Falconet Denis, Maréchal Eric.* Adaptive traits of cysts of the snow alga *Sanguina nivaloides* unveiled by 3D subcellular imaging // *Nature Communications*. XI 2023. 14, 1. 7500. Publisher: Nature
- 830 Publishing Group.
- Flanner M. G., Liu X., Zhou C., Penner J. E., Jiao C.* Enhanced solar energy absorption by internally-mixed black carbon in snow grains // *Atmospheric Chemistry and Physics*. V 2012. 12, 10. 4699–4721. Publisher: Copernicus GmbH.
- Flanner Mark G., Arnheim Julian B., Cook Joseph M., Dang Cheng, He Cenlin, Huang Xianglei, Singh Deepak, Skiles S. McKenzie, Whicker Chloe A., Zender Charles S.* SNICAR-ADv3: a community tool for modeling spectral snow albedo // *Geoscientific Model Development*.
- 835 XII 2021. 14, 12. 7673–7704. Publisher: Copernicus GmbH.
- Flanner Mark G., Zender Charles S., Randerson James T., Rasch Philip J.* Present-day climate forcing and response from black carbon in snow // *Journal of Geophysical Research: Atmospheres*. 2007. 112, D11. _eprint: <https://onlinelibrary.wiley.com/doi/pdf/10.1029/2006JD008003>.
- Gabbi J., Huss M., Bauder A., Cao F., Schwikowski M.* The impact of Saharan dust and black carbon on albedo and long-term mass balance
- 840 of an Alpine glacier // *The Cryosphere*. VII 2015. 9, 4. 1385–1400. Publisher: Copernicus GmbH.
- Gardner Alex S., Sharp Martin J.* A review of snow and ice albedo and the development of a new physically based broadband albedo parameterization // *Journal of Geophysical Research: Earth Surface*. 2010. 115, F1. _eprint: <https://onlinelibrary.wiley.com/doi/pdf/10.1029/2009JF001444>.
- Gascoïn Simon, Grizonnet Manuel, Bouchet Marine, Salgues Germain, Hagolle Olivier.* Theia Snow collection: high-resolution operational
- 845 snow cover maps from Sentinel-2 and Landsat-8 data // *Earth System Science Data*. IV 2019. 11, 2. 493–514. Publisher: Copernicus GmbH.
- Gascoïn Simon, Soubeyroux Jean-Michel, Karbou Fatima, Thirel Guillaume, Sourp Laura, Lejeune Yves, Gouttevin Isabelle, Morin Samuel.* Évolution du manteau neigeux pendant la sécheresse de 2022 en France // *LHB*. XII 2024. 110, 1. 2314174. Publisher: Taylor & Francis _eprint: <https://doi.org/10.1080/27678490.2024.2314174>.
- 850 *Gerbaux M., Genthon C., Etchevers P., Vincent C., Dedieu J. P.* Surface mass balance of glaciers in the French Alps: distributed modeling and sensitivity to climate change // *Journal of Glaciology*. I 2005. 51, 175. 561–572. Publisher: Cambridge University Press.
- Gilardoni S., Di Mauro B., Bonasoni P.* Black carbon, organic carbon, and mineral dust in South American tropical glaciers: A review // *Global and Planetary Change*. VI 2022. 213. 103837.
- Gilbert A., Gimbert F., Gagliardini O., Vincent C.* Inferring the Basal Friction Law From Long Term Changes of Glacier Length, Thickness and Velocity on an Alpine Glacier // *Geophysical Research Letters*. 2023. 50, 16. e2023GL104503. _eprint: <https://onlinelibrary.wiley.com/doi/pdf/10.1029/2023GL104503>.
- Ginot P., Dumont M., Lim S., Patris N., Taupin J.-D., Wagnon P., Gilbert A., Arnaud Y., Marinoni A., Bonasoni P., Laj P.* A 10 year record of black carbon and dust from a Mera Peak ice core (Nepal): variability and potential impact on melting of Himalayan glaciers // *The Cryosphere*. VIII 2014. 8, 4. 1479–1496. Publisher: Copernicus GmbH.

- 860 *Ginoux Paul, Chin Mian, Tegen Ina, Prospero Joseph M., Holben Brent, Dubovik Oleg, Lin Shian-Jiann.* Sources and distributions of dust aerosols simulated with the GOCART model // *Journal of Geophysical Research: Atmospheres*. 2001. 106, D17. 20255–20273. _eprint: <https://onlinelibrary.wiley.com/doi/pdf/10.1029/2000JD000053>.
- Grange Stuart K., Lötscher Hanspeter, Fischer Andrea, Emmenegger Lukas, Hueglin Christoph.* Evaluation of equivalent black carbon source apportionment using observations from Switzerland between 2008 and 2018 // *Atmospheric Measurement Techniques*. IV 2020. 13, 4. 865 1867–1885. Publisher: Copernicus GmbH.
- Gunnarsson Andri, Gardarsson Sigurdur M., Pálsson Finnur.* Modeling of surface energy balance for Icelandic glaciers using remote-sensing albedo // *The Cryosphere*. IX 2023. 17, 9. 3955–3986. Publisher: Copernicus GmbH.
- Günther Daniel, Marke Thomas, Essery Richard, Strasser Ulrich.* Uncertainties in Snowpack Simulations—Assessing the Impact of Model Structure, Parameter Choice, and Forcing Data Error on Point-Scale Energy Balance Snow Model Performance // *Water Resources Research*. 2019. 55, 4. 2779–2800. _eprint: <https://onlinelibrary.wiley.com/doi/pdf/10.1029/2018WR023403>.
- 870 *Hagolle Olivier, Huc Mireille, Villa Pascual David, Dedieu Gerard.* A Multi-Temporal and Multi-Spectral Method to Estimate Aerosol Optical Thickness over Land, for the Atmospheric Correction of FormoSat-2, LandSat, VEN μ S and Sentinel-2 Images // *Remote Sensing*. III 2015. 7, 3. 2668–2691. Number: 3 Publisher: Multidisciplinary Digital Publishing Institute.
- He Cenlin, Flanner Mark G., Chen Fei, Barlage Michael, Liou Kuo-Nan, Kang Shichang, Ming Jing, Qian Yun.* Black carbon-induced snow albedo reduction over the Tibetan Plateau: uncertainties from snow grain shape and aerosol–snow mixing state based on an updated 875 SNICAR model // *Atmospheric Chemistry and Physics*. VIII 2018. 18, 15. 11507–11527. Publisher: Copernicus GmbH.
- Kneib Marin, Dehecq Amaury, Brun Fanny, Karbou Fatima, Charrier Laurane, Leinss Silvan, Wagnon Patrick, Maussion Fabien.* Mapping and characterization of avalanches on mountain glaciers with Sentinel-1 satellite imagery // *The Cryosphere*. VI 2024a. 18, 6. 2809–2830. Publisher: Copernicus GmbH.
- 880 *Kneib Marin, Dehecq Amaury, Gilbert Adrien, Basset Auguste, Miles Evan S., Juvet Guillaume, Jourdain Bruno, Ducasse Etienne, Beraud Luc, Rabatel Antoine, Mougnot Jérémie, Carcanade Guillem, Laarman Olivier, Brun Fanny, Six Delphine.* Distributed surface mass balance of an avalanche-fed glacier // *EGUphere*. VII 2024b. 1–35. Publisher: Copernicus GmbH.
- Lafaysse Matthieu, Cluzet Bertrand, Dumont Marie, Lejeune Yves, Vionnet Vincent, Morin Samuel.* A multiphysical ensemble system of numerical snow modelling // *The Cryosphere*. V 2017. 11, 3. 1173–1198. Publisher: Copernicus GmbH.
- 885 *Lamboll Robin D., Jones Chris D., Skeie Ragnhild B., Fiedler Stephanie, Samset Bjørn H., Gillett Nathan P., Rogelj Joeri, Forster Piers M.* Modifying emissions scenario projections to account for the effects of COVID-19: protocol for CovidMIP // *Geoscientific Model Development*. VI 2021. 14, 6. 3683–3695. Publisher: Copernicus GmbH.
- Lejeune Yves, Bouilloud Ludovic, Etchevers Pierre, Wagnon Patrick, Chevallier Pierre, Sicart Jean-Emmanuel, Martin Eric, Habets Florence.* Melting of Snow Cover in a Tropical Mountain Environment in Bolivia: Processes and Modeling // *Journal of Hydrometeorology*. VIII 2007. 8, 4. 922–937. Publisher: American Meteorological Society Section: Journal of Hydrometeorology.
- 890 *Liang Shunlin, Shuey Chad J, Russ Andrew L, Fang Hongliang, Chen Mingzhen, Walthall Charles L, Daughtry Craig S. T, Hunt Raymond.* Narrowband to broadband conversions of land surface albedo: II. Validation // *Remote Sensing of Environment*. I 2003. 84, 1. 25–41.
- Magalhães Newton de, Evangelista Heitor, Condom Thomas, Rabatel Antoine, Ginot Patrick.* Amazonian Biomass Burning Enhances Tropical Andean Glaciers Melting // *Scientific Reports*. XI 2019. 9, 1. 16914. Publisher: Nature Publishing Group.
- 895 *Menounos Brian, Huss Matthias, Marshall Shawn, Ednie Mark, Florentine Caitlyn, Hartl Lea.* Glaciers in Western Canada-Conterminous US and Switzerland Experience Unprecedented Mass Loss Over the Last Four Years (2021–2024) // *Geophysical Research Letters*. 2025. 52, 12. e2025GL115235. _eprint: <https://agupubs.onlinelibrary.wiley.com/doi/pdf/10.1029/2025GL115235>.

- Michou M., Nabat P., Saint-Martin D.* Development and basic evaluation of a prognostic aerosol scheme (v1) in the CNRM Climate Model CNRM-CM6 // *Geoscientific Model Development*. III 2015. 8, 3. 501–531. Publisher: Copernicus GmbH.
- 900 *Michou M., Nabat P., Saint-Martin D., Bock J., Decharme B., Mallet M., Roehrig R., Séférian R., Sénési S., Voldoire A.* Present-Day and Historical Aerosol and Ozone Characteristics in CNRM CMIP6 Simulations // *Journal of Advances in Modeling Earth Systems*. 2020. 12, 1. e2019MS001816. _eprint: <https://agupubs.onlinelibrary.wiley.com/doi/pdf/10.1029/2019MS001816>.
- Mittelberger Simon, Soubeyroux Jean-Michel, Batté Lauriane.* La sécheresse 2022 en France : retour vers le futur // *LHB*. XII 2024. 110, 1. 2304351. Publisher: Taylor & Francis _eprint: <https://doi.org/10.1080/27678490.2024.2304351>.
- 905 *Morcrette J.-J., Boucher O., Jones L., Salmond D., Bechtold P., Beljaars A., Benedetti A., Bonet A., Kaiser J. W., Razinger M., Schulz M., Serrar S., Simmons A. J., Sofiev M., Suttie M., Tompkins A. M., Untch A.* Aerosol analysis and forecast in the European Centre for Medium-Range Weather Forecasts Integrated Forecast System: Forward modeling // *Journal of Geophysical Research: Atmospheres*. 2009. 114, D6. _eprint: <https://agupubs.onlinelibrary.wiley.com/doi/pdf/10.1029/2008JD011235>.
- Moulin C., Lambert C. E., Dayan U., Masson V., Ramonet M., Bousquet P., Legrand M., Balkanski Y. J., Guelle W., Marticorena B., Bergametti G., Dulac F.* Satellite climatology of African dust transport in the Mediterranean atmosphere // *Journal of Geophysical Research: Atmospheres*. 1998. 103, D11. 13137–13144. _eprint: <https://onlinelibrary.wiley.com/doi/pdf/10.1029/98JD00171>.
- Ménégoz M., Krinner G., Balkanski Y., Boucher O., Cozic A., Lim S., Ginot P., Laj P., Gallée H., Wagnon P., Marinoni A., Jacobi H. W.* Snow cover sensitivity to black carbon deposition in the Himalayas: from atmospheric and ice core measurements to regional climate simulations // *Atmospheric Chemistry and Physics*. IV 2014. 14, 8. 4237–4249. Publisher: Copernicus GmbH.
- 915 *Möller Rebecca, Dagsson-Waldhauserova Pavla, Möller Marco, Kukla Peter A., Schneider Christoph, Gudmundsson Magnús T.* Persistent albedo reduction on southern Icelandic glaciers due to ashfall from the 2010 Eyjafjallajökull eruption // *Remote Sensing of Environment*. XI 2019. 233. 111396.
- Nabat Pierre, Somot Samuel, Cassou Christophe, Mallet Marc, Michou Martine, Bouniol Dominique, Decharme Bertrand, Drugé Thomas, Roehrig Romain, Saint-Martin David.* Modulation of radiative aerosols effects by atmospheric circulation over the Euro-Mediterranean region // *Atmospheric Chemistry and Physics*. VII 2020. 20, 14. 8315–8349. Publisher: Copernicus GmbH.
- 920 *Naegeli Kathrin, Huss Matthias.* Sensitivity of mountain glacier mass balance to changes in bare-ice albedo // *Annals of Glaciology*. VII 2017. 58, 75pt2. 119–129. Publisher: Cambridge University Press.
- O'Rourke Patrick, Smith Steven, Mott Andrea, Ahsan Hamza, McDuffie Erin, Crippa Monica, Klimont Zbigniew, McDonald Brian, Wang Shuxiao, Nicholson Matthew, Hoesly Rachel, Feng Leyang.* CEDS v_2021_04_21 Gridded emissions data. 2021.
- 925 *Oerlemans J., Giesen R. H., Broeke M. R. Van Den.* Retreating alpine glaciers: increased melt rates due to accumulation of dust (Vadret da Morteratsch, Switzerland) // *Journal of Glaciology*. I 2009. 55, 192. 729–736.
- Painter Thomas H., Seidel Felix C., Bryant Ann C., McKenzie Skiles S., Rittger Karl.* Imaging spectroscopy of albedo and radiative forcing by light-absorbing impurities in mountain snow // *Journal of Geophysical Research: Atmospheres*. 2013. 118, 17. 9511–9523. _eprint: <https://onlinelibrary.wiley.com/doi/pdf/10.1002/jgrd.50520>.
- 930 *Picard Ghislain, Libois Quentin.* Simulation of snow albedo and solar irradiance profile with the Two-streAm Radiative TransfEr in Snow (TARTES) v2.0 model // *Geoscientific Model Development*. XII 2024. 17, 24. 8927–8953. Publisher: Copernicus GmbH.
- Qian Yun, Wang Hailong, Zhang Rudong, Flanner Mark G., Rasch Philip J.* A sensitivity study on modeling black carbon in snow and its radiative forcing over the Arctic and Northern China // *Environmental Research Letters*. VI 2014. 9, 6. 064001. Publisher: IOP Publishing.
- Rabatel Antoine, Sanchez Olivier, Vincent Christian, Six Delphine.* Estimation of Glacier Thickness From Surface Mass Balance and Ice Flow Velocities: A Case Study on Argentière Glacier, France // *Frontiers in Earth Science*. VIII 2018. 6. Publisher: Frontiers.
- 935

- Raleigh M. S., Lundquist J. D., Clark M. P.* Exploring the impact of forcing error characteristics on physically based snow simulations within a global sensitivity analysis framework // *Hydrology and Earth System Sciences*. VII 2015. 19, 7. 3153–3179. Publisher: Copernicus GmbH.
- 940 *Randerson J. T., Werf G. R. van der, Giglio L., Collatz G. J., Kasibhatla P. S.* Global Fire Emissions Database, Version 4.1 (GFEDv4) // ORNL Distributed Active Archive Center (DAAC) dataset 10.3334/ORNLDAAC/1293 (2017. I 2017. 1293. ADS Bibcode: 2017ornl.data.1293R.
- Revuelto Jesús, Lecourt Grégoire, Lafaysse Matthieu, Zin Isabella, Charrois Luc, Vionnet Vincent, Dumont Marie, Rabatel Antoine, Six Delphine, Condom Thomas, Morin Samuel, Viani Alessandra, Sirguey Pascal.* Multi-Criteria Evaluation of Snowpack Simulations in Complex Alpine Terrain Using Satellite and In Situ Observations // *Remote Sensing*. VIII 2018. 10, 8. 1171. Number: 8 Publisher: Multidisciplinary Digital Publishing Institute.
- 945 *Robledano Alvaro, Picard Ghislain, Arnaud Laurent, Larue Fanny, Ollivier Inès.* Modelling surface temperature and radiation budget of snow-covered complex terrain // *The Cryosphere*. II 2022. 16, 2. 559–579. Publisher: Copernicus GmbH.
- Roussel Léon, Dumont Marie, Gascoïn Simon, Monteiro Diego, Bavay Mathias, Nabat Pierre, Ezzedine Jade Abdellatif, Fructus Mathieu, Lafaysse Matthieu, Morin Samuel, Maréchal Eric.* Snowmelt duration controls red algal blooms in the snow of the European Alps // *Proceedings of the National Academy of Sciences*. X 2024. 121, 41. e2400362121. Publisher: Proceedings of the National Academy of
- 950 *Sciences.*
- Réveillet Marion, Dumont Marie, Gascoïn Simon, Lafaysse Matthieu, Nabat Pierre, Ribes Aurélien, Nheili Rafife, Tuzet Francois, Ménégoz Martin, Morin Samuel, Picard Ghislain, Ginoux Paul.* Black carbon and dust alter the response of mountain snow cover under climate change // *Nature Communications*. IX 2022. 13, 1. 5279. Number: 1 Publisher: Nature Publishing Group.
- Réveillet Marion, Six Delphine, Vincent Christian, Rabatel Antoine, Dumont Marie, Lafaysse Matthieu, Morin Samuel, Vionnet Vincent, Litt*
- 955 *Maxime.* Relative performance of empirical and physical models in assessing the seasonal and annual glacier surface mass balance of Saint-Sorlin Glacier (French Alps) // *The Cryosphere*. IV 2018. 12, 4. 1367–1386. Publisher: Copernicus GmbH.
- Sarangi Chandan, Qian Yun, Rittger Karl, Ruby Leung L., Chand Duli, Bormann Kat J., Painter Thomas H.* Dust dominates high-altitude snow darkening and melt over high-mountain Asia // *Nature Climate Change*. XI 2020. 10, 11. 1045–1051. Publisher: Nature Publishing Group.
- 960 *Schwarz J. P., Gao R. S., Perring A. E., Spackman J. R., Fahey D. W.* Black carbon aerosol size in snow // *Scientific Reports*. III 2013. 3, 1. 1356. Publisher: Nature Publishing Group.
- Shaw Thomas E., Buri Pascal, McCarthy Michael, Miles Evan S., Ayala Álvaro, Pellicciotti Francesca.* The Decaying Near-Surface Boundary Layer of a Retreating Alpine Glacier // *Geophysical Research Letters*. 2023. 50, 11. e2023GL103043. _eprint: <https://onlinelibrary.wiley.com/doi/pdf/10.1029/2023GL103043>.
- 965 *Shaw Thomas E., Buri Pascal, McCarthy Michael, Miles Evan S., Pellicciotti Francesca.* Local Controls on Near-Surface Glacier Cooling Under Warm Atmospheric Conditions // *Journal of Geophysical Research: Atmospheres*. 2024. 129, 2. e2023JD040214. _eprint: <https://onlinelibrary.wiley.com/doi/pdf/10.1029/2023JD040214>.
- Shea Joseph Michael.* Regional-scale distributed modelling of glacier meteorology and melt, southern Coast Mountains, Canada. 2010.
- Sicart Jean Emmanuel, Hock Regine, Six Delphine.* Glacier melt, air temperature, and energy balance in different climates: The Bolivian Tropics, the French Alps, and northern Sweden // *Journal of Geophysical Research: Atmospheres*. 2008. 113, D24. _eprint: <https://onlinelibrary.wiley.com/doi/pdf/10.1029/2008JD010406>.
- 970 *Six Delphine, Vincent Christian, Bonnefoy-Demongeot Mylène, Thibert Emmanuel, René Pierre.* 2022 : année record pour la fonte des glaciers français // *La Météorologie*. 2023. 2023, 120. 13–15.

- Skiles S. McKenzie, Flanner Mark, Cook Joseph M., Dumont Marie, Painter Thomas H. Radiative forcing by light-absorbing particles in snow // *Nature Climate Change*. XI 2018. 8, 11. 964–971. Publisher: Nature Publishing Group.
- 975 Sun Jia, Birmili Wolfram, Hermann Markus, Tuch Thomas, Weinhold Kay, Merkel Maik, Rasch Fabian, Müller Thomas, Schladitz Alexander, Bastian Susanne, Löschau Gunter, Cyrus Josef, Gu Jianwei, Flentje Harald, Briel Björn, Asbach Christoph, Kaminski Heinz, Ries Ludwig, Sohmer Ralf, Gerwig Holger, Wirtz Klaus, Meinhardt Frank, Schwerin Andreas, Bath Olaf, Ma Nan, Wiedensohler Alfred. Decreasing trends of particle number and black carbon mass concentrations at 16 observational sites in Germany from 2009 to 2018 // *Atmospheric Chemistry and Physics*. VI 2020. 20, 11. 7049–7068. Publisher: Copernicus GmbH.
- 980 Thibert E., Blanc R., Vincent C., Eckert N. Glaciological and volumetric mass-balance measurements: error analysis over 51 years for Glacier de Sarennes, French Alps // *Journal of Glaciology*. I 2008. 54, 186. 522–532.
- Tuzet Francois, Dumont Marie, Lafaysse Matthieu, Picard Ghislain, Arnaud Laurent, Voisin Didier, Lejeune Yves, Charrois Luc, Nabat Pierre, Morin Samuel. A multilayer physically based snowpack model simulating direct and indirect radiative impacts of light-absorbing impurities in snow // *The Cryosphere*. XI 2017. 11, 6. 2633–2653. Publisher: Copernicus GmbH.
- 985 Tuzet François, Dumont Marie, Picard Ghislain, Lamare Maxim, Voisin Didier, Nabat Pierre, Lafaysse Mathieu, Larue Fanny, Revuelto Jesus, Arnaud Laurent. Quantification of the radiative impact of light-absorbing particles during two contrasted snow seasons at Col du Lautaret (2058 m a.s.l., French Alps) // *The Cryosphere*. XII 2020. 14, 12. 4553–4579. Publisher: Copernicus GmbH.
- Vernay Matthieu, Lafaysse Matthieu, Monteiro Diego, Hagenmuller Pascal, Nheili Raffaele, Samacoïts Raphaëlle, Verfaillie Deborah, Morin Samuel. The S2M meteorological and snow cover reanalysis over the French mountainous areas: description and evaluation (1958–2021) // *Earth System Science Data*. IV 2022. 14, 4. 1707–1733. Publisher: Copernicus GmbH.
- 990 Vincent C., Soruco A., Six D., Meur E. Le. Glacier thickening and decay analysis from 50 years of glaciological observations performed on Glacier d’Argentière, Mont Blanc area, France // *Annals of Glaciology*. I 2009. 50, 50. 73–79.
- Vionnet V., Brun E., Morin S., Boone A., Faroux S., Le Moigne P., Martin E., Willemet J.-M. The detailed snowpack scheme Crocus and its implementation in SURFEX v7.2 // *Geoscientific Model Development*. V 2012. 5, 3. 773–791. Publisher: Copernicus GmbH.
- 995 Vionnet Vincent, Six Delphine, Auger Ludovic, Dumont Marie, Lafaysse Matthieu, Quéno Louis, Réveillet Marion, Dombrowski-Etchevers Ingrid, Thibert Emmanuel, Vincent Christian. Sub-kilometer Precipitation Datasets for Snowpack and Glacier Modeling in Alpine Terrain // *Frontiers in Earth Science*. VIII 2019. 7. Publisher: Frontiers.
- Warren Stephen G. Optical properties of snow // *Reviews of Geophysics*. 1982. 20, 1. 67–89. [_eprint: https://onlinelibrary.wiley.com/doi/pdf/10.1029/RG020i001p00067](https://onlinelibrary.wiley.com/doi/pdf/10.1029/RG020i001p00067).
- 1000 Warren Stephen G. Impurities in Snow: Effects on Albedo and Snowmelt (Review) // *Annals of Glaciology*. I 1984. 5. 177–179.
- Warren Stephen G. Light-Absorbing Impurities in Snow: A Personal and Historical Account // *Frontiers in Earth Science*. I 2019. 6. Publisher: Frontiers.
- Whicker Chloe A., Flanner Mark G., Dang Cheng, Zender Charles S., Cook Joseph M., Gardner Alex S. SNICAR-ADv4: a physically based radiative transfer model to represent the spectral albedo of glacier ice // *The Cryosphere*. IV 2022. 16, 4. 1197–1220. Publisher: Copernicus GmbH.
- 1005